© 2024. Published by The Company of Biologists Ltd | Disease Models & Mechanisms (2024) 17, dmm050740. doi:10.1242/dmm.050740

RESOURCES & METHODS

Human organoid model of pontocerebellar hypoplasia 2a recapitulates brain region-specific size differences

Theresa Kagermeier[1,2], Stefan Hauser[1,3], Kseniia Sarieva[1,2,4], Lucia Laugwitz[5], Samuel Groeschel[5], Wibke G. Janzarik[6], Zeynep Yentür[1,2,4,7], Katharina Becker[1], Ludger Schöls[1,3], Ingeborg Krägeloh-Mann[5] and Simone Mayer[1,7,*,‡]

ABSTRACT

Pontocerebellar hypoplasia type 2a (PCH2a) is an ultra-rare, autosomal recessive pediatric disorder with limited treatment options. Its anatomical hallmark is hypoplasia of the cerebellum and pons accompanied by progressive microcephaly. A homozygous founder variant in *TSEN54*, which encodes a tRNA splicing endonuclease (TSEN) complex subunit, is causal. The pathological mechanism of PCH2a remains unknown due to the lack of a model system. Therefore, we developed human models of PCH2a using regionalized neural organoids. We generated induced pluripotent stem cell (iPSC) lines from three males with genetically confirmed PCH2a and subsequently differentiated cerebellar and neocortical organoids. Mirroring clinical neuroimaging findings, PCH2a cerebellar organoids were reduced in size compared to controls starting early in differentiation. Neocortical PCH2a organoids demonstrated milder growth deficits. Although PCH2a cerebellar organoids did not upregulate apoptosis, their stem cell zones showed altered proliferation kinetics, with increased proliferation at day 30 and reduced proliferation at day 50 compared to controls. In summary, we generated a human model of PCH2a, providing the foundation for deciphering brain region-specific disease mechanisms. Our first analyses suggest a neurodevelopmental aspect of PCH2a.

KEY WORDS: Organoid, PCH2a, Apoptosis, Cerebellum, Differentiation, Rare disease

INTRODUCTION

Pontocerebellar hypoplasias (PCHs) are a heterogeneous group of neurogenetic disorders characterized by severe neurodevelopmental impairment and hypoplasia of the cerebellum and pons (van Dijk et al., 2018). Besides the primary pontocerebellar hypoplasia, affected individuals develop progressive microcephaly (Barth et al., 2007; Namavar et al., 2011). PCH2 is the most common form of PCH but it is still ultra-rare (estimated 1:100,000 births) (Budde et al., 2008; Sanchez-Albisua et al., 2014). Clinically, PCH2 is characterized by profound neurodevelopmental delay, causing a significant burden to affected individuals and their families (Ammann-Schnell et al., 2021; Sanchez-Albisua et al., 2014). To date, no curative treatment is available, and disease management is focused on alleviating symptoms.

Ninety percent of PCH2 cases are caused by a homozygous founder variant in the *TSEN54* gene (OMIM *608755; NM_207346.3: c.919G>T, p.Ala307Ser) and are referred to as PCH2a (OMIM #277470) (Budde et al., 2008; van Dijk et al., 2018). *TSEN54* encodes a subunit of the tRNA splicing endonuclease (TSEN) complex, which is involved in excising introns from a subset of pre-tRNAs by providing structural support and mediating substrate recognition (Chan and Lowe, 2009; Trotta et al., 2006; Yuan et al., 2023; Zhang et al., 2023). The TSEN54 protein region that contains the Ala307Ser variant is not visualized by single-particle cryogenic electron microscopy, suggesting that it is unstructured (Hayne et al., 2023; Sekulovski et al., 2023). Although bi-allelic pathogenic variants in *TSEN54* do not affect the endonuclease activity of the TSEN complex in fibroblasts of affected individuals, they result in a thermal destabilization of the complex and altered tRNA pools (Sekulovski et al., 2021). The TSEN54 protein is expressed throughout the body at varying levels (Human Protein Atlas) (Uhlen et al., 2015). At the mRNA level, *TSEN54* is widely expressed in the developing human brain (Human Brain Transcriptome) (Kang et al., 2011) starting in the first trimester of gestation (Kasher et al., 2011). In the second trimester of gestation, *TSEN54* is expressed highly in the developing cerebellum, pons and olivary nuclei (Budde et al., 2008). Its expression does not appear to be cell type-specific in the developing neocortex and cerebellum at the level of mRNA (Aldinger et al., 2021; Nowakowski et al., 2017). Collectively, from the TSEN54 expression pattern alone, it is unclear why specifically the cerebellum and pons are affected in PCH2a (Kasher et al., 2011). Interestingly, additional variants in *TSEN54* (associated with PCH4 and PCH5), as well as variants in other subunits of the TSEN complex (associated with PCH2b, PCH2c and PCH2f) and variants in *CLP1* (associated with PCH10), which encodes a protein that interacts with the TSEN complex, result in clinical phenotypes related to PCH2a (Schaffer et al., 2019). Therefore, it has been hypothesized that specific brain areas are especially vulnerable to TSEN malfunction due to a specific requirement of this complex during perinatal and early postnatal development (Budde et al., 2008).

---

[1]Hertie Institute for Clinical Brain Research, University of Tübingen, 72076 Tübingen, Germany. [2]Graduate Training Centre of Neuroscience, University of Tübingen, 72076 Tübingen, Germany. [3]German Center for Neurodegenerative Diseases, 72076 Tübingen, Germany. [4]International Max Planck Research School, Graduate Training Centre of Neuroscience, University of Tübingen, 72076 Tübingen, Germany. [5]Department of Neuropediatrics, Developmental Neurology and Social Pediatrics, University of Tübingen, 72076 Tübingen, Germany. [6]Department of Neuropediatrics and Muscle Disorders, Center for Pediatrics and Adolescent Medicine, Medical Center, Faculty of Medicine, University of Freiburg, 79106 Freiburg, Germany. [7]Heidelberger Akademie der Wissenschaften, 69117 Heidelberg, Germany.

*Present address: Zoological Institute and the Institute of Biological and Chemical Systems – Functional Molecular Systems, Karlsruhe Institute of Technology, Karlsruhe, Germany.

‡Authors for correspondence (si.mayer@uni-tuebingen.de; simone.mayer@kit.edu)

T.K., 0000-0002-7557-8523; S.H., 0000-0002-1022-7482; K.S., 0000-0002-0579-6090; L.L., 0000-0003-2506-1961; S.G., 0000-0002-2706-7163; W.G.J., 0000-0002-3651-1385; Z.Y., 0000-0002-4832-9927; K.B., 0000-0002-6479-3762; L.S., 0000-0001-7774-5025; I.K.-M., 0000-0003-4599-1373; S.M., 0000-0002-6381-2474

Handling Editor: Steven J. Clapcote
Received 31 January 2024; Accepted 13 May 2024

Histopathological analysis to date has revealed a reduced complexity of cerebellar foliation, patches of Bergmann glia, loss of Purkinje cells (PCs), and severely reduced and misplaced granule cells (GCs), the major neuronal cell types of the cerebellar cortex (Rudnik-Schöneborn et al., 2014). Efforts to recapitulate PCH2a in animal models have not determined the cellular mechanism of pathophysiology so far (Schmidt et al., 2022; Kasher et al., 2011). Although the TSEN complex is conserved from archaea, *TSEN54* has undergone evolutionary changes in the primate lineage (Lee et al., 2016). Notably, the amino acid sequence around *TSEN54*: c.919G>T (p.Ala307Ser) is not conserved between species (Budde et al., 2008). Of the frequently used model organisms, only mouse and chicken share the amino acid residue (Budde et al., 2008). A recently developed fly model of PCH shows defects in brain development, death at larval stages and apoptosis upon loss of function of the *TSEN54* ortholog, but the relevance to the brain region-specific clinical phenotype is unclear (Schmidt et al., 2022). In zebrafish, loss of *tsen54* function leads to cell death in the brain during development (Kasher et al., 2011). A complete loss of *Tsen54* in mice results in early embryonic lethality (Ermakova et al., 2018). Moreover, a bi-allelic missense variant of *TSEN54* in dogs leads to a neurological disorder characterized by leukodystrophy, a disease with a strikingly different pathophysiology (Stork et al., 2019). These findings imply a potential species-specific effect of TSEN54 malfunction on brain development. Additionally, the brain has changed tremendously in evolution, especially in the primate lineage (Herculano-Houzel, 2012). Compared to the mouse neocortex, the human neocortex has expanded dramatically (1000× in the number of neurons and surface area), has a protracted development (neurogenesis is 20× longer than in mouse) and displays an unprecedented cellular heterogeneity (Geschwind and Rakic, 2013; Miller et al., 2019). Similarly, the human cerebellum has a 750-fold greater surface area than that of the mouse cerebellum, a protracted development occurring over 2-3 years compared to 30-35 days in mice, and additional transient stem cell zones that cannot be found in mice (Haldipur et al., 2022). Taken together, the lack of appropriate models of PCH2a has to date precluded the elucidation of its cellular and molecular pathology.

As an alternative to animal models, human brain organoid models have recently been increasingly used to model neurodevelopmental and early-onset neurodegenerative disorders as well as investigating environmental impacts on brain development (Eichmüller and Knoblich, 2022; Sarieva and Mayer, 2021). In order to study brain region-specific biology, it is possible to guide the differentiation of organoids to a specific brain region by adding specific morphogens (Fleck et al., 2021; Kadoshima et al., 2013; Sloan et al., 2018). Neocortical organoids, for instance, recapitulate cell type composition of the developing human neocortex with $SOX2^+$ ventricular radial glia cells organized into rosettes reminiscent of the ventricular zone (VZ) and shed other neural progenitor cells (NPCs) and neurons to putative subventricular zone and cortical plate regions, respectively (Pasca et al., 2015). Within the cortical plate-like regions, a distinct lamination pattern emerges, featuring CTIP2 $(BCL11B)^+$ deep-layer and $SATB2^+$ upper-layer excitatory neurons (Pasca et al., 2015).

Similarly, in cerebellar organoid differentiation protocols (Muguruma et al., 2015; Silva et al., 2020), the stem cells of two cerebellar NPC zones are established: $KIRREL2^+/PTF1A^+$ VZ and $BARHL1^+/ATOH1^+$ rhombic lip (RL) (Leto et al., 2016; Mizuhara et al., 2010). These NPCs generate neurons of two major cerebellar neuronal identities: PCs and GCs, respectively. PC precursors ($KIRREL2^+/PTF1A^+$) are derived from the VZ and identified by OLIG2/SKOR2 expression, and subsequently mature into calbindin (CALB or $CALB1)^+$ PCs. (Leto et al., 2016; Wang et al., 2011). RL-derived precursors ($BARHL1^+/ATOH1^+$) differentiate into GCs and glutamatergic deep cerebellar nuclei neurons, which are positive for LHX2 (Ballabio et al., 2020; Kamei et al., 2023; Lago et al., 2023; Morales and Hatten, 2006).

In this study, we leveraged the recent developments in the generation of regionalized neural organoids (Zhang et al., 2022) to create a human model of PCH2a. We identified three individuals that display the genetic, clinical and brain imaging features previously described for PCH2a. We then derived induced pluripotent stem cells (iPSCs) from donated fibroblasts (Fig. 1A) from these three affected children and three healthy individuals (all male, Table 1). We did not find differences in proliferation and cell death between PCH2a and control iPSCs. Next, we differentiated PCH2a and control iPSCs towards a cerebellar and neocortical fate in three-dimensional (3D) cultures. Growth curves of organoids recapitulated the brain region-specific pathology observed in affected individuals. Cerebellar PCH2a organoids were severely reduced in size compared to controls starting early in differentiation, whereas neocortical PCH2a organoids showed less severe divergence from controls only at later stages of differentiation. We did not detect differences in the induction of apoptosis in NPCs. Instead, we found an increased number and thickness of neural rosettes along with increased proliferation in these areas in early but not late differentiation stages in PCH2a cerebellar organoids compared to controls. Our study thus provides first insights into the disease mechanism, which can be analyzed in depth in future studies by using the *in vitro* models of PCH2a established here.

RESULTS

Generation of PCH2a-derived iPSCs

It is unclear how a ubiquitously expressed gene involved in tRNA metabolism causes pathology only in specific tissues and even within the nervous system, with differential pathology in different brain regions. Based on recent successes in modeling neurogenetic disorders in organoids (Khakipoor et al., 2020; Velasco et al., 2020), we reasoned that a human iPSC-based regionalized neural organoid model could recapitulate pathological hallmarks of PCH2a (Fig. 1A). Previously, cerebellar organoids were used to investigate the mechanisms of medulloblastoma, a pediatric cerebellar cancer (Ballabio et al., 2020; Lago et al., 2023). We hypothesized that generating neocortical organoids and cerebellar organoids might model the brain region-specific pathology in PCH2a. To our knowledge, cerebellar organoids have not yet been used to model neurogenetic disorders involving the cerebellum.

As a first step, we recruited three affected males (Fig. 1B,C) with genetically confirmed PCH2a, harboring the c.919G>T variant in the *TSEN54* gene in the homozygous state (Fig. 1D). Clinical features typical of PCH2a (Sanchez-Albisua et al., 2014) were evident in all probands (Table S1). In summary, subjects displayed severe developmental delay with minimal cognitive and motor development, seizures of variable semiology and a severe dystonic movement disorder. Moreover, the probands exhibited dysphagia and gastrointestinal disturbances (Table S1). Neuroimaging revealed severe hypoplasia of the brainstem, pons and cerebellum in contrast to less severe volume reduction of the cerebrum, as seen in an affected child (donor of iPSC line PCH02) (Fig. 1C) in comparison to an age-matched control (Fig. 1B).

We obtained skin biopsies from these three probands, extracted fibroblasts and derived iPSCs using an episomal reprogramming approach (Fig. 1A) (Okita et al., 2013). iPSCs were subjected to a

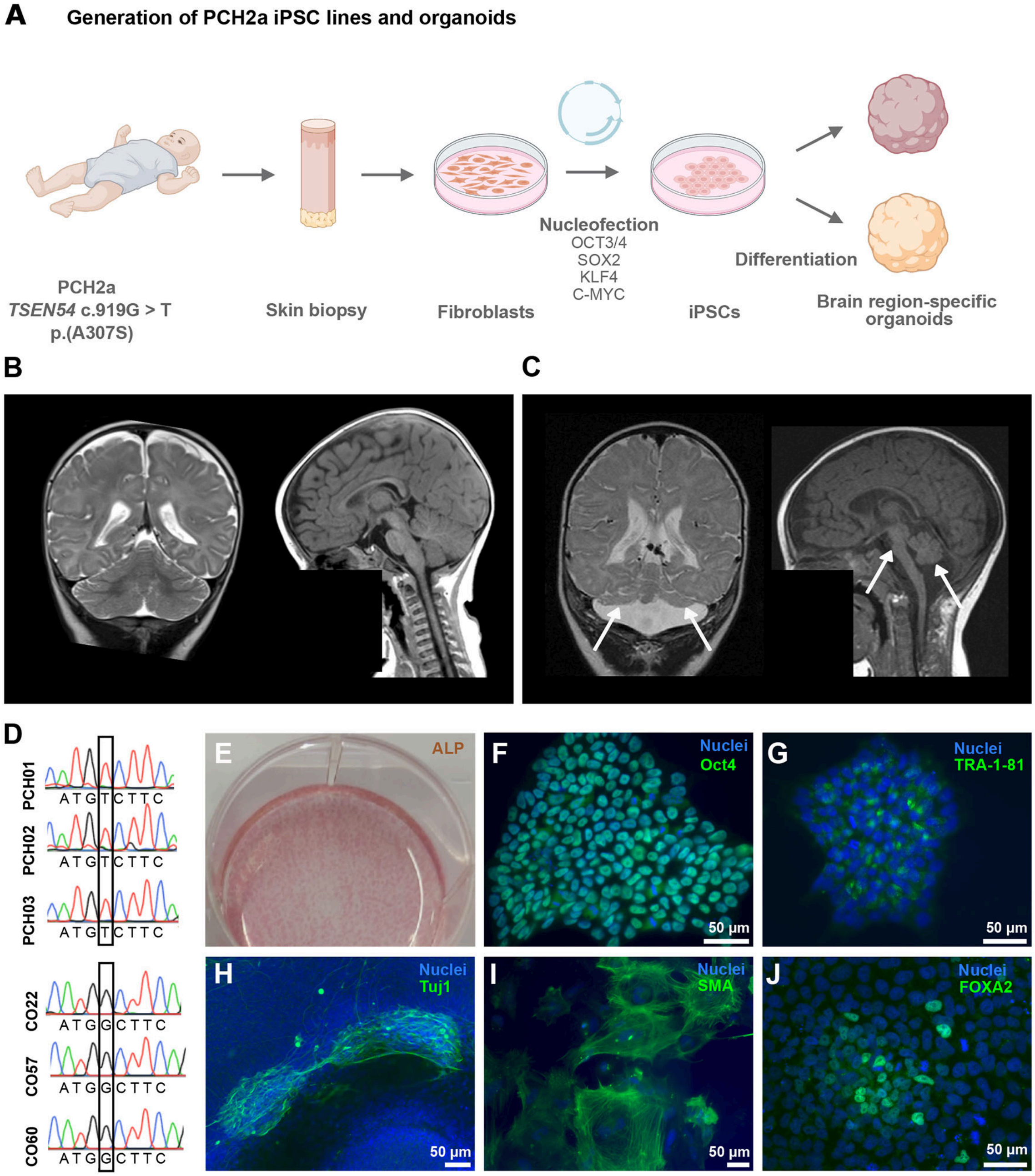

Fig. 1. Generation of PCH2a iPSCs. (A) Experimental scheme of PCH2a induced pluripotent stem cell (iPSC) generation (scheme was created with BioRender.com). (B) Magnetic resonance imaging (MRI) scans of the brain of a normally developing infant (6 months of age) and (C) an infant with PCH2a (6 months of age, donor of iPSC line PCH02). T2-weighted coronal images (B,C, left) show cerebellar hemispheres severely reduced in size (indicated by arrows) in the PCH2a child compared to the control individual. T1-weighted sagittal images (B,C, right) illustrate the severe pontine and cerebellar hypoplasia in the PCH2a child (indicated by arrows). The facial regions of the MRI scans are covered in order to protect the privacy of both individuals. (D) Sanger sequencing results of PCH2a iPSCs verifies the *TSEN54* c.919G>T point mutation, whereas control lines show the c.919G genotype (homozygous). (E) Alkaline phosphatase (ALP) staining of undifferentiated iPSCs. (F,G) Immunocytochemical staining of undifferentiated iPSCs for the pluripotency markers OCT4 (F) and TRA-1-81 (G) and DAPI (nuclei) demonstrates the pluripotency of generated cell lines. (H-J) Immunocytochemical staining of iPSCs spontaneously differentiated into the three germ layers illustrates the differentiation potential of the generated iPSCs. Cells were stained for Tuj1 (tubulin βIII marker, ectoderm) (H), smooth muscle actin (SMA, mesoderm) (I) and forkhead box A2 (FOXA2, endoderm) (J), as well as DAPI (nuclei). Representative images show iPSCs from the cell line PCH01.

range of quality controls. First, pluripotency was confirmed through staining for alkaline phosphatase (ALP) (Fig. 1E) and immunocytochemistry for OCT4 and the TRA-1-81 antigen podocalyxin (PODXL) (Fig. 1F,G). The differentiation potential was corroborated using spontaneous tri-lineage differentiation (Korneck et al., 2022). iPSCs differentiated into the three primordial germ layers, namely, the ectoderm (marked by the Tuj1 antibody against tubulin βIII or TUBB3), the mesoderm (identified by an antibody against smooth muscle actin or SMA) and the endoderm (identified by anti-FOXA2) (Fig. 1H-J). Control lines used in this study were generated following the same protocol and were subjected to all aforementioned quality controls (see Materials

Table 1. Origins of iPSC lines

Cell line ID	Donor age	Ethnicity	Sex	Pathogenic *TSEN54* variant
CO22	74 years	European	Male	c.[919=];[919=]
CO57	46 years	European	Male	c.[919=];[919=]
CO60	22 years	European	Male	c.[919=];[919=]
PCH01	9 months	European	Male	c.919G>T; c.919G>T
PCH02	14 years	European	Male	c.919G>T; c.919G>T
PCH03	4 years	European	Male	c.919G>T; c.919G>T

and Methods for a detailed description). Single nucleotide polymorphism (SNP) array analysis of all six lines used in this study revealed no larger chromosomal aberrations induced by the reprogramming (Data S1). Additionally, control lines did not harbor the c.919G>T variant (Fig. 1D).

In order to determine even subtle differences in iPSC properties between PCH2a and control lines, we assessed and quantified the number of cells expressing the pluripotency marker OCT4 (Fig. 2A,B), the proliferative marker Ki67 (MKI67) (Fig. 2C,D) and the apoptotic marker cleaved caspase-3 (cCas3; encoded by *CASP3*) (Fig. 2E,F) of three consecutive passages of all PCH2a and control iPSC lines used in this study. We identified no significant differences in the number of cells expressing these markers between PCH2a and control lines. Additionally, we incubated the iPSC lines with 5-ethynyl-2′-deoxyuridine (EdU) for 1 and 4 h to assess the proliferation rate (Fig. 2G,H). Quantification of EdU$^+$ cells revealed no significant difference in EdU incorporation between PCH2a and control lines. In conclusion, the pathogenic variant does not affect the proliferation and viability of the iPSCs. indicating that iPSCs derived from affected individuals maintain characteristics of control iPSC lines and can be used for studying tissue-specific pathology by employing regionalized neural organoid differentiation protocols.

Human brain organoids have brain region-specific growth deficits

To model brain region-specific pathology, we then differentiated three control and the three PCH2a iPSC lines into cerebellar (Silva et al., 2020) and neocortical organoids (Pasca et al., 2015) (formally referred to as cortical spheroids; Pasca et al., 2022) using established protocols (Fig. 3A).

We first determined whether cerebellar hypoplasia and progressive microcephaly found in affected individuals (Fig. 1B,C) were recapitulated in our *in vitro* model (Fig. 3B,C). We therefore measured the sizes of both cerebellar and neocortical organoids in brightfield images at day (D) 10, D20, D30, D50, D70 and D90. During neocortical differentiation, one PCH2a line was contaminated and the differentiation was terminated at D20. Interestingly, for both brain region-specific differentiations, we found significant differences in size between PCH2a and control organoids (Fig. 3A-C; Fig. S1A-F). On average, cerebellar PCH2a organoids were smaller than controls starting from D10 of differentiation (Fig. 3B), whereas neocortical PCH2a organoids showed differences from D30 onwards (Fig. 3C). Statistical assessment (three-way ANOVA) revealed no significant difference for the sizes within the two experimental groups (PCH2a or control) at any time point, justifying the comparison of mean sizes between groups. Linear regression models were significantly different between control and PCH2a organoids of both regional identities (Fig. S1G,H, Table S2). At D50, the ratio between the mean sizes of control and PCH2a cerebellar organoids was 1.85, increasing to 3.12 at D90 (Fig. 3D). In neocortical organoids, the ratio between the mean sizes of control and PCH2a organoids was 1.13 at D50 and 1.74 at D90 of differentiation (Fig. 3D). The regionalized neural organoid growth curves resembled brain morphometry in PCH2a-affected individuals with early detection of cerebellar hypoplasia in the first months of life (Sanchez-Albisua et al., 2014) and later progressive microcephaly (Ekert et al., 2016), albeit at a different time scale.

PCH2a-derived iPSCs differentiate towards cerebellar and neocortical fate

To start assessing the cellular underpinnings of the brain region-specific growth deficits (Fig. 3), we analyzed the presence of different progenitor and neuronal cell types in cerebellar and neocortical organoids at different time points in PCH2a and control organoids. We found robust neural differentiation in both PCH2a and control cerebellar organoids based on immunohistochemical analysis for the markers SOX2 (NPCs) and Tuj1 (immature neurons) at D30 (Fig. 4A,B). Moreover, cerebellar organoids demonstrated the presence of both RL- and VZ-derived cerebellar NPC populations. Immunohistochemistry against BARHL1 (Fig. 4A,B) and ATOH1 (Fig. S2A-D) confirmed the presence of RL-derived glutamatergic cerebellar precursor cells. Cerebellar VZ derivates such as GABAergic cerebellar precursors are characterized by KIRREL2 (Fig. 4C,D), OLIG2 (Fig. S2E,F) and SKOR2 (Fig. S3A-D) in immunohistochemistry at D30. At later stages of differentiation (D90), we found CALB- and MAP2-positive cells, indicating the presence of PCs in cerebellar organoids (Fig. 4E,F). Similarly, in neocortical organoids, immunohistochemical analysis for CTIP2, SATB2, SOX2 and Tuj1 collectively revealed neocortical differentiation and generation of layer-specific excitatory neurons (Fig. S3A-F). We found expression of the NPC marker SOX2 in neural rosettes surrounded by CTIP2-positive deep-layer excitatory neurons at D50 in control (Fig. S3A) and PCH2a (Fig. S3B) neocortical organoids. In addition, expression of the upper-layer excitatory neuron marker SATB2 was found at D70 and D90 (Fig. S3C-F). Taken together, the acquisition of regionalized neural fate and neuronal maturation was evident in both cerebellar and neocortical control and PCH2a organoids, suggesting that they can be used to analyze molecular and cellular changes induced by the disease-causing variant.

Expression of the apoptotic marker cCas3 is not altered in PCH2a cerebellar and neocortical organoids

Previous histopathological assessment of a PCH2a-affected individual suggested a degenerative nature of the disease (Barth et al., 2007; Rudnik-Schöneborn et al., 2014). Additionally, studies on zebrafish and fruit fly *TSEN54* ortholog loss-of-function models indicated that hypoplasia resulted from cell death (Kasher et al., 2011; Schmidt et al., 2022). We therefore investigated whether elevated levels of apoptosis could explain the reduced size of PCH2a cerebellar and neocortical organoids. However, immunohistochemistry for the apoptotic marker cCas3 did not reveal differences between control and PCH2a cerebellar (Fig. 5A) and neocortical (Fig. 5B) organoids. Quantitative analysis of the cCas3-positive area over the DAPI-positive area of individual regions of interest (ROIs) (SOX2-rich regions containing SOX2$^+$ rosettes and surrounding cells) did not show a significant difference between PCH2a and control organoids at D30 and D50 in both cerebellar (Fig. 5C) and neocortical (Fig. 5D) organoids. Further quantification of the cCas3$^+$ area within the SOX2$^+$ area only did not show elevated apoptosis in the SOX2$^+$ NPC population either (Fig. 5E,F). Taken together, we observed a significant size difference in PCH2a brain organoids (Fig. 3) in the absence of

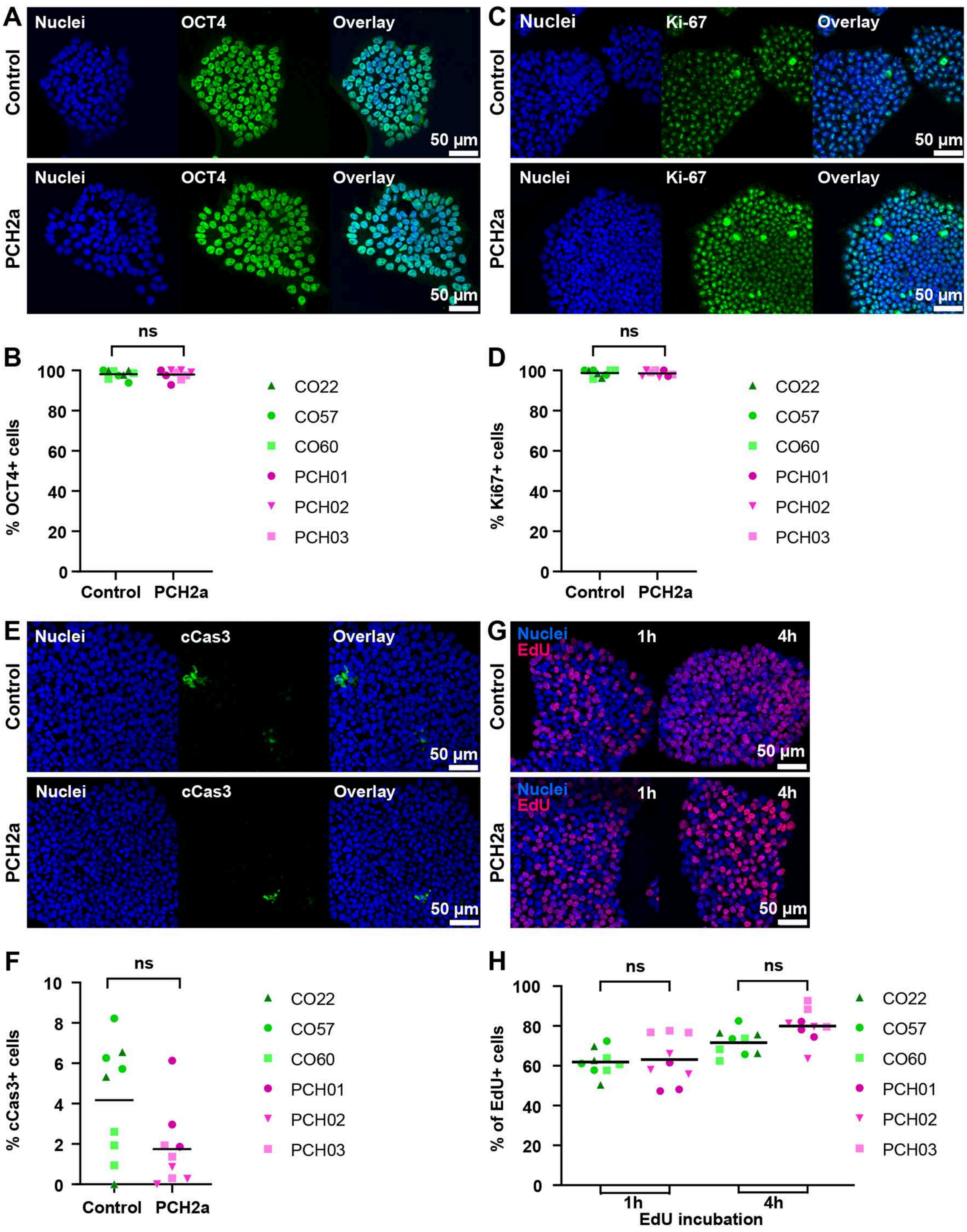

Fig. 2. PCH2a-derived and control iPSCs do not differ in expression of pluripotency, proliferation and apoptosis markers. (A,C) Immunocytochemical staining of PCH2a and control iPSCs for the pluripotency marker OCT4 (A) and the proliferation marker Ki67 (C) confirmed their expression in all iPSC lines [representative images are of iPSCs from the cell lines CO22, passage (P) 19, and PCH01, P17 (A), and CO57, P20, and PCH03, P20 (B)]. (B,D) Quantification of OCT4$^+$ cells (B) and Ki67$^+$ cells (D) normalized to DAPI-based cell count showed no significant difference in the number of OCT4$^+$ or Ki67$^+$ cells between PCH2a and control iPSCs (assessment of three passages per cell line). (E) Immunocytochemical staining of PCH2a and control iPSCs for the apoptosis marker cCas3 showed low expression levels in all iPSC lines (representative images are of iPSCs from CO60, P18, and PCH02, P18). (F) Quantification of cCas3$^+$ cells, normalized to DAPI-based cell count showed no significant difference in number of cCas3$^+$ cells between PCH2a and control iPSCs (assessment of three passages per cell line). (G) Visualization of cell proliferation by click-chemistry detection of EdU in PCH2a and control iPSCs after 1 and 4 h of incubation with EdU (representative images are of iPSCs from CO60, P18, and PCH02, P18). (H) Quantification of EdU-positive cells, normalized to DAPI-based cell count after 1 and 4 h of EdU incubation showed no significant difference in the number of EdU-positive cells between PCH2a and control iPSCs (assessment of three passages per cell line). ns, $P>0.05$ [two-tailed unpaired *t*-test with Welch's correction assuming unequal standard deviations (SDs)].

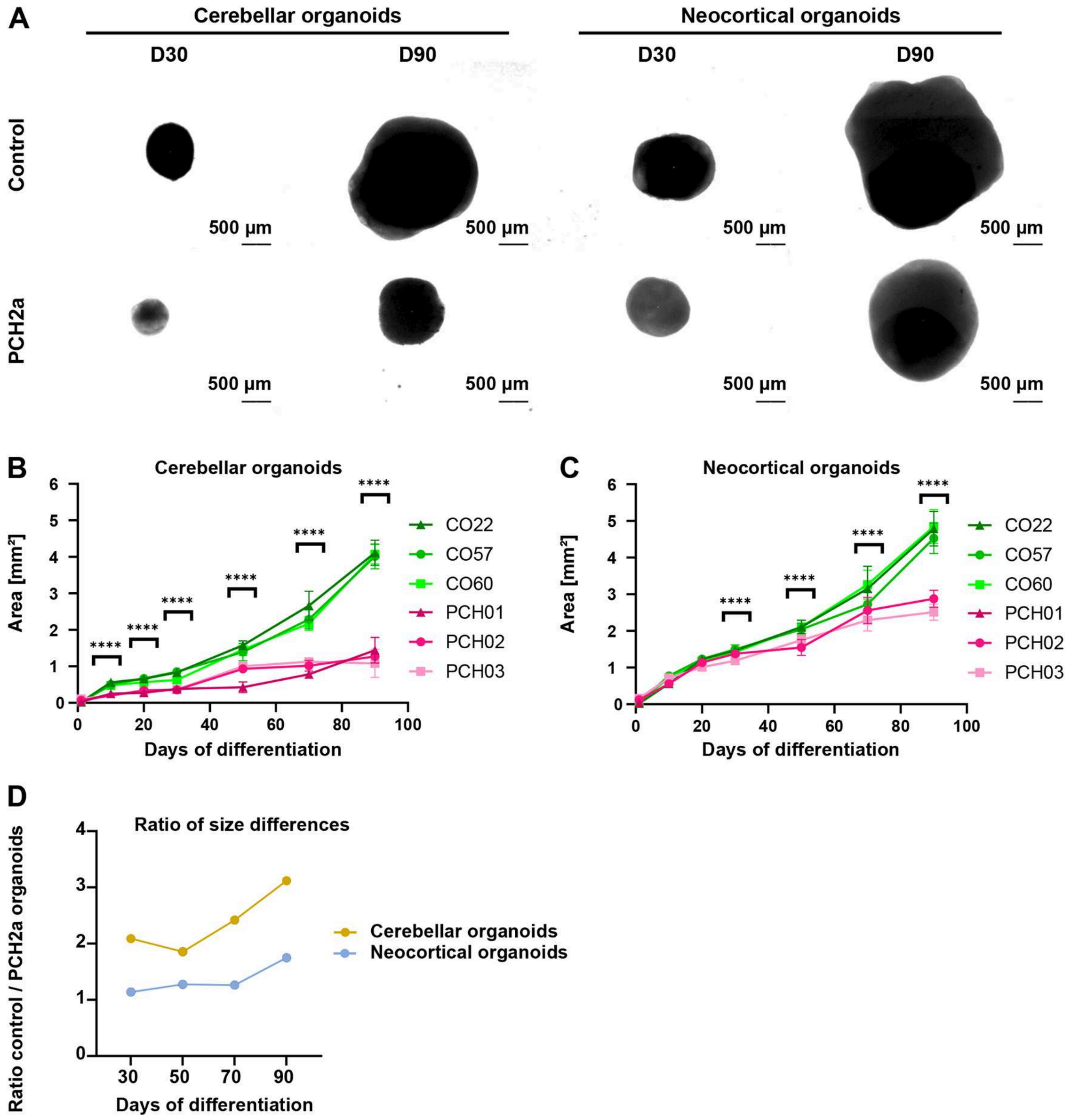

Fig. 3. PCH2a organoids are significantly smaller than control organoids. (A) Representative brightfield images of cerebellar and neocortical organoids in culture at day (D) 30 and D90 of differentiation illustrate the differences in size. (B,C) Growth curves of PCH2a and control cerebellar (B) and neocortical (C) organoids, differentiated from three different cell lines per condition (derived from three different individuals), show the area of the organoids in the images pictured in A during the culture period of 90 days. Cerebellar organoids (B) differed significantly in size from D10 of differentiation, with discrepancies increasing over time. Neocortical organoids (C) showed significant differences from D30 of differentiation. *n*>8 organoids per cell line, timepoint and differentiation. Note that PCH01 neocortical differentiation is absent due to a contamination. Points represent the mean, error bars represent s.e.m. ****$P<0.05$ (two-tailed unpaired *t*-test with Welch's correction assuming unequal SDs). (D) The ratio between mean sizes of control and PCH2a organoids calculated from data presented in B,C. The ratios increased over time and were higher within cerebellar differentiation.

obvious changes in apoptosis at D30 and D50 of differentiation in cerebellar and neocortical organoids (Fig. 5).

PCH2a cerebellar organoids show earlier establishment of dense SOX2$^+$ structures

Instead of apoptosis, an alternative hypothesis that could explain the reduced size of cerebellar and neocortical organoids is altered proliferation of NPCs. We therefore assessed possible changes in SOX2$^+$ NPCs through immunohistochemistry. Analysis at D30 and D50 of differentiation showed that the number and structure of SOX2$^+$-rich rosette structures differed between PCH2a and control cerebellar organoids (Fig. 6A) with no apparent differences in neocortical organoids (Fig. 6B). In D30 PCH2a cerebellar organoids, SOX2$^+$ rosettes took up 24±3.07% (mean±s.e.m.) of the total organoid area, whereas in control, only 2±0.53% of the organoid area was taken up by SOX2$^+$ rosettes (Fig. 6C). At D50, this difference was reversed: control cerebellar organoids showed a larger area of SOX2$^+$ structures over the total organoid area (12±1.24%) than PCH2a organoids (2±0.92%). In contrast, neocortical organoids did not show differences in the area of SOX2$^+$ rosette structures over the total organoid area on both D30 and D50 of differentiation (Fig. 6D). As they differentiated from D30 to D50, the percentage of SOX2$^+$ rosettes increased in both PCH2a and control neocortical organoids (Fig. 6D).

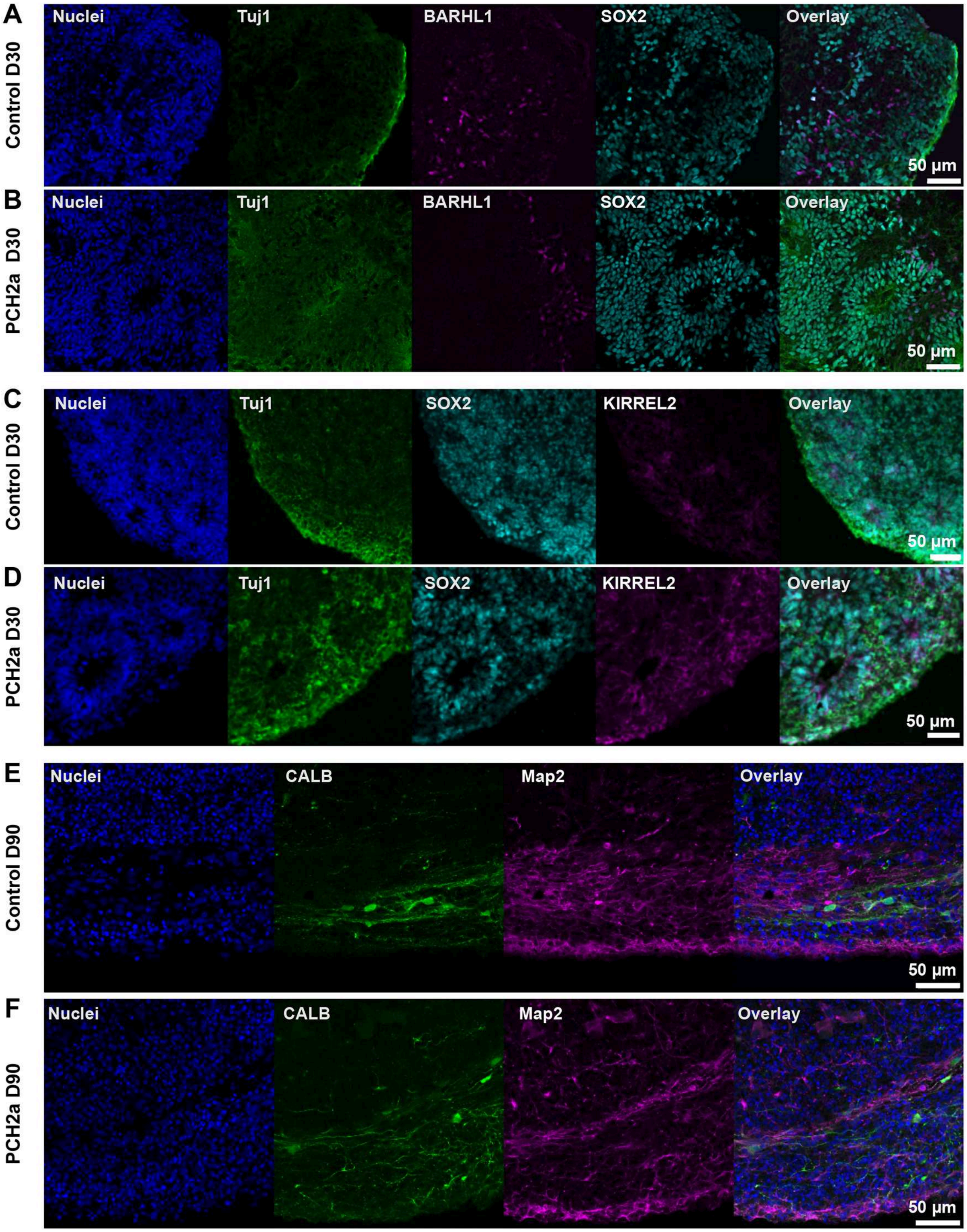

Fig. 4. PCH2a and control cerebellar organoids show differentiation into the cerebellar lineage. Immunohistochemistry of control and PCH2a cerebellar organoid sections at D30 and D90 showed differentiation into the cerebellar lineage. (A,B) Expression of the early neuronal marker Tuj1 (green), the neural precursor marker SOX2 (cyan) and the glutamatergic precursor marker BARHL1 (magenta) in D30 control (A) and PCH2a (B) cerebellar organoids (representative images show organoids derived from CO22, P19, and PCH02, P17). (C,D) The GABA-ergic precursor marker KIRREL2 (magenta) is expressed in D30 cerebellar control (C) and PCH2a (D) organoids together with Tuj1 (green) and SOX2 (cyan) (representative images are of iPSCs from CO22, P19, and PCH01, P19). (E,F) Control (E) and PCH2a (I) cerebellar organoids show calbindin (CALB, cyan) in postmitotic Purkinje cells and neuronal marker MAP2 (magenta) expression (representative images are of iPSCs from CO57, P18, and PCH03, P19).

Different factors such as morphogen gradients or viral infections can influence the morphology of SOX2$^+$ structures in brain organoids (Albanese et al., 2020; Pagliaro et al., 2023). To determine whether SOX2$^+$ rosette structures also possessed a distinct morphology in cerebellar PCH2a organoids, we quantified the average size and thickness of the SOX2$^+$ structures. At D30 of differentiation, PCH2a cerebellar organoids had significantly bigger and thicker SOX2$^+$ structures than those of controls; this difference was reversed at D50 (Fig. S4A,C). Neocortical PCH2a organoids did not show significant differences in the size of SOX2$^+$ structures

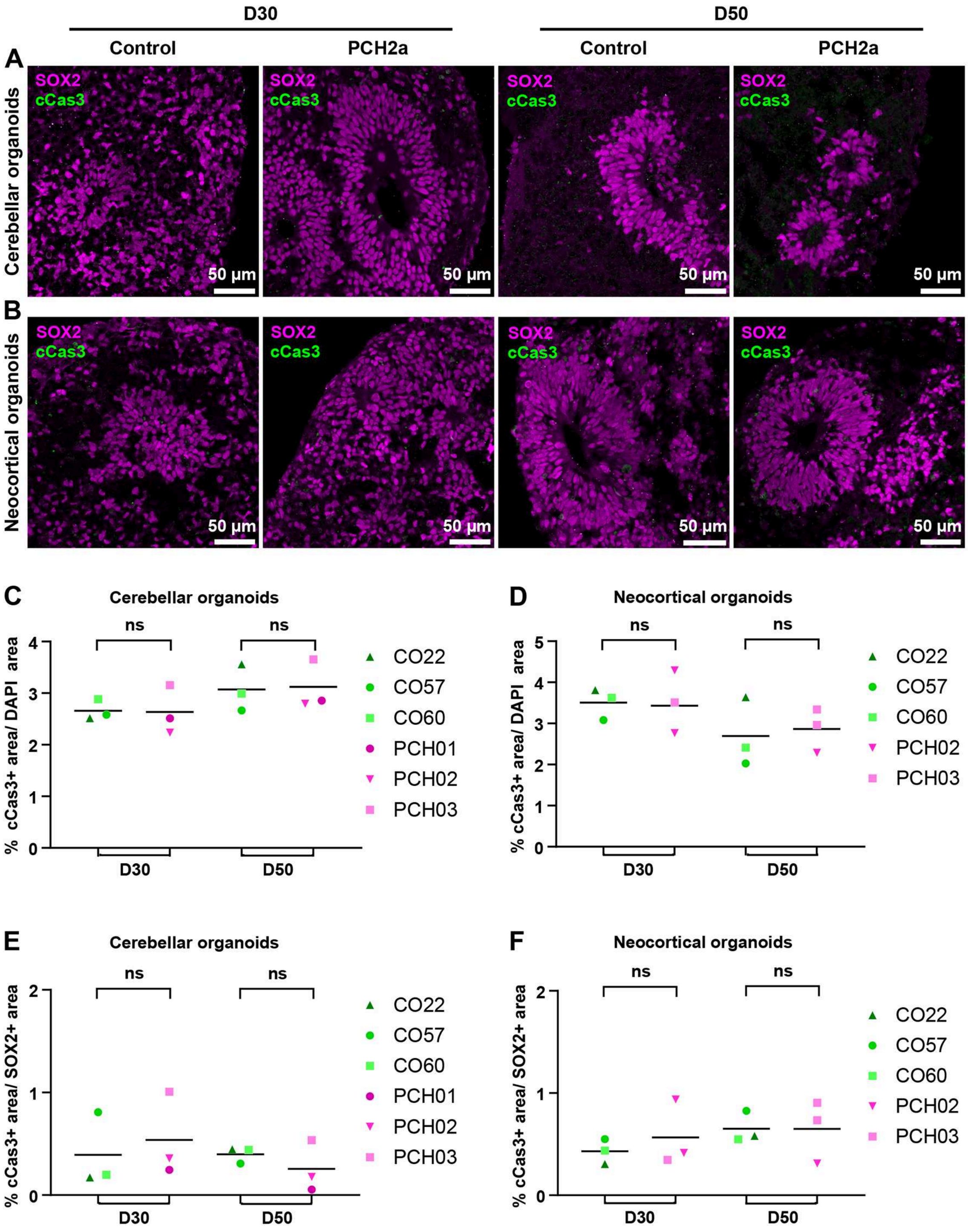

Fig. 5. Expression of the apoptotic marker cCas3 is not altered in PCH2a organoids. (A,B) Confocal microscopy images of immunohistochemistry on cerebellar (A) and neocortical (B) organoid sections at D30 and D50 of differentiation show expression of the neural precursor marker SOX2 and the apoptotic marker cCas3 in rosette-like structures of organoids. Representative images of cerebellar organoids (A) are from CO22, P19, and PCH03, P19 (D30/D50), and those for neocortical organoids (B) are from CO57, P18, and PCH02, P17 (D30/50). (C,D) Quantification of the cCas3-positive area over DAPI signal showed no significant difference in cCas3 expression between PCH2a and control in cerebellar (C) and neocortical (D) organoids at D30 and D50 of differentiation. (E,F) Quantification of cCas3-positive area within the SOX2$^+$ area showed no significant difference in cCas3 expression between PCH2a and control in cerebellar (E) and neocortical (F) organoids at D30 and D50 of differentiation. ns, not significant, P>0.05 (two-tailed unpaired t-test with Welch's correction assuming unequal SDs).

at D30 or D50 of differentiation compared to controls (Fig. S4B). There was a slight reduction in the thickness of SOX2$^+$ structures in PCH2a neocortical organoids compared to those in controls at D30 (Fig. S4D), but not at D50 (Fig. S4D). To investigate whether the altered SOX2$^+$ rosette structures in cerebellar and neocortical organoids also translated to higher proliferation within these structures, we quantified the proportion of Ki67$^+$ cells among SOX2$^+$ cells (Fig. 6E,F). We found higher proliferation of the

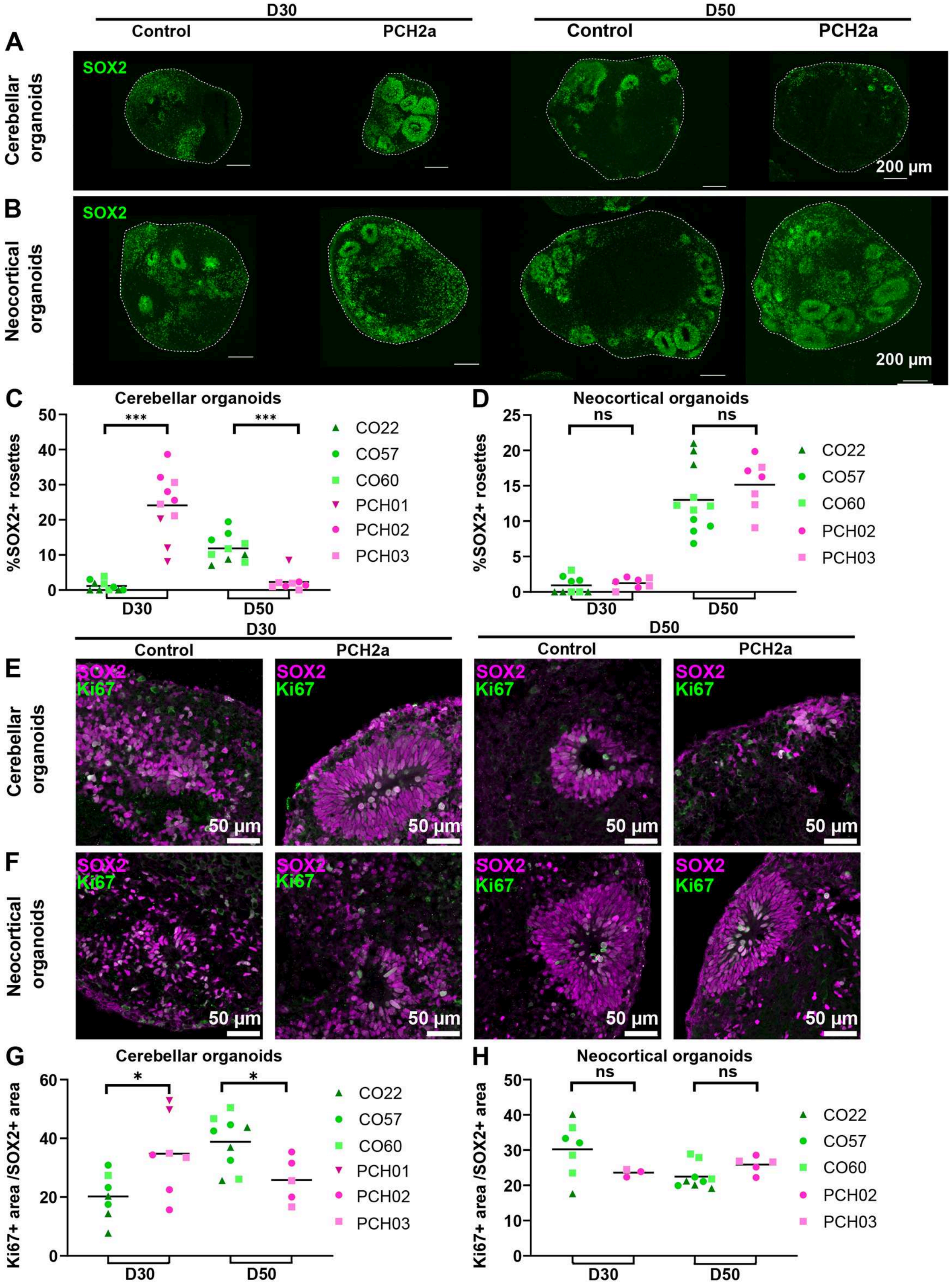

Fig. 6. See next page for legend.

SOX2$^+$ cells (Fig. 6G) in D30 PCH2a cerebellar organoids compared to that in controls. Conversely, the proliferation of SOX2$^+$ cells was lower in D50 PCH2a cerebellar organoids compared to that in controls (Fig. 6G). We did not find any differences in the proportion of Ki67$^+$/SOX2$^+$ cells between PCH2a and control neocortical organoids (Fig. 6H). Taken together, these analyses indicate aberrant proliferation properties of the NPCs in cerebellar organoids. In line with the severity of the growth deficit (Fig. 3), dramatic changes in progenitor cell properties were seen in PCH2a cerebellar organoids compared to controls, whereas only subtle differences were found in neocortical organoids when comparing PCH2a and control differentiations. Taken together, we propose that size differences between PCH2a and control lines in cerebellar and neocortical organoids are explained predominantly by proliferation differences rather than increased apoptosis.

Fig. 6. PCH2a cerebellar organoids show earlier establishment of dense SOX2$^+$ structures, whereas neocortical organoids demonstrate no difference in SOX2$^+$ structures. (A,B) Epifluorescence images of immunohistochemistry on cerebellar (A) and neocortical (B) organoids at D30 and D50 of differentiation show the expression of SOX2 (NPCs) in control (left) and PCH2a (right) organoids. Representative images of cerebellar organoids (A) are from CO57, P18, and PCH02, P17 (D30); and CO57, P18, and PCH03, P19 (D50); those for neocortical organoids (B) are from CO57, P18, and PCH02 P17 (D30); and CO22, P19, and PCH02, P17 (D50). (C,D) Quantitative analysis of the area covered by SOX2$^+$ structures normalized to the area of the organoid. (C) PCH2a cerebellar organoids showed a significantly higher proportion of dense SOX2$^+$ structures at D30, whereas control organoids showed these structures at D50. (D) Neocortical organoids did not show significant differences at D30 and D50. (E,F) Confocal images of immunohistochemistry against Ki67 (magenta) and Tuj1 (green) in cerebellar (E) and neocortical (F) organoid sections at D50 illustrate the expression of Ki67 in PCH2a (right) and control (left) organoids within SOX2$^+$ structures. Representative images for cerebellar organoids (E) are from CO57, P18, and PCH03, P19 (D30); and CO57, P18, and PCH03, P19 (D50); and those for neocortical organoids (F) are from CO60, P19, and PCH02, P17 (D30); and CO60, P19, and PCH02, P17 (D50). The PCH2a cerebellar organoid at D30 is also used to illustrate quantification in Fig. S5A-C. (G,H) Quantitative analysis of percentage of Ki67$^+$ area normalized to SOX2$^+$ area in cerebellar and neocortical organoids at D30 and D50 of differentiation. (G) PCH2a cerebellar organoids showed a significantly higher proportion of Ki67$^+$ area at D30. This difference was reversed at D50 of differentiation. (H) Neocortical organoids did not demonstrate significant differences at D30 and D50 of differentiation in the Ki67$^+$/SOX2$^+$ area. ns, not significant, $P>0.05$; *$P<0.05$; ***$P<0.001$ (two-tailed unpaired *t*-test with Welch's correction assuming unequal SDs).

DISCUSSION

Understanding the cellular and molecular mechanisms of PCH2a has been hampered to date by the lack of a model replicating neuroanatomical hallmarks of the disorder such as the brain region-specific hypoplasia. Moreover, no study to date has modeled the specific variant underlying PCH2a in a neural cellular context. In this study, we aimed to close this gap by generating human brain region-specific organoid models of PCH2a. To achieve that, we (1) derived three iPSC lines from affected individuals (Fig. 1), (2) compared these lines with three control iPSC lines generated by the same protocol (Figs 1 and 2), and (3) extensively characterized PCH2a and control iPSC-derived cerebellar and neocortical organoids (Figs 3–6) to start elucidating the mechanisms underlying cerebellar hypoplasia and microcephaly. We found that, although PCH2a-derived iPSCs did not differ from control lines (Fig. 2), both cerebellar and neocortical organoids demonstrated disease-relevant phenotypes. Thus, we propose that human regionalized brain organoids can serve as models to study cellular and molecular mechanisms underlying PCH2a in a tissue-specific manner.

Using patient-derived iPSCs to model rare diseases

An important consideration in light of the current study is the suitability of using patient-derived iPSCs for disease modeling *in vitro*. A major concern in this context is the reproducibility between iPSC lines derived from non-related individuals with distinct genetic backgrounds. It has been reported that the major source of variation between different iPSC lines is their genetic background (Volpato and Webber, 2020). Genetic background inevitably differs between PCH2a-derived and control cell lines and thus serves as a technical confounder that may increase variation (Volpato and Webber, 2020). It may also allow overlooking additional genetic variants that affect the disease course but were missed in the causal gene identification. In order to mitigate such confounding effects, we analyzed iPSC properties in detail (Fig. 2) and found no differences between PCH2a and control lines. In our organoid differentiations, we also achieved robust differences between the PCH2a and control lines despite the genetic differences. Importantly, PCH2a is a genetically homogenous disorder, characterized by a single homozygous missense mutation, and may thus be particularly suited to such an experimental design. Furthermore, we did not find significant differences in organoid sizes within the control or PCH2a group (Fig. 3). The fact that we can generate highly reproducible data while using cell lines derived from unrelated individuals can also be seen as a strength of our study. The lack of genetic engineering using CRISPR-Cas9 also means that no off-target effects can confound our results. In conclusion, although we show consistent results between the three control lines and the three PCH2a lines, respectively, an important extension of our study will be to confirm our findings in isogenic cell lines.

Brain region-specific anatomical hallmarks recapitulated in organoids

In individuals affected by PCH2a, a cerebellum reduced in size is already present at birth, whereas a progressive reduction of cerebral volumes may be detected with time, suggesting an ongoing atrophic process of neurodegeneration (Ekert et al., 2016). Analogously, we found that cerebellar PCH2a organoids were severely reduced in size from early stages on, whereas neocortical PCH2a organoids started displaying differences in growth at later stages of development (Fig. 3). Additionally, differences in cerebellar organoid size between PCH2a and controls at later stages were larger compared to those for neocortical PCH2a and control organoids (Fig. 3). In patients, the atrophy of supratentorial structures could be either caused by a primary effect of the disease-causing variant or a consequence of the lack of inputs from the cerebellum, as has been discussed in studies of very preterm infants with cerebellar lesions (Limperopoulos et al., 2014). Our data on the reduced size of neocortical organoids starting at D30 of differentiation indicate that the disease-causing *TSEN54* variant directly affects neocortical development. We therefore suggest that primary as well as secondary effects of the pathogenic variant on cerebellar and neocortical development may contribute to the diverse clinical phenotype of PCH2a. Notably, just 20% of the human cerebellum is involved in motor function (Haldipur et al., 2022; Marek et al., 2018), and cerebellar hypoplasia disrupting cerebellar–cerebral projections may, thus, also contribute directly to the pathological hallmarks of PCH2a not related to motor function, such as neurodevelopmental delay and lack of language development.

Novel insights into the disease mechanism of PCH2a using the organoid models

Our model provides the foundation for studying the cellular and molecular disease mechanisms underlying PCH2a as we can generate species-specific biomaterial with regionalized neural fate for subsequent analysis of the biochemical and cellular differences. Elucidating the mechanisms of PCH2a has implications for PCH subtypes that are caused by variants in TSEN genes and *CLP1* (Schaffer et al., 2019). Furthermore, it can further be relevant for other rare neurological disorders caused by defects in the tRNA-processing machinery (Schaffer et al., 2019).

Mutations in *TSEN54* lead to aberrant tRNA pools in human fibroblasts (Sekulovski et al., 2021). Assuming that aberrant tRNA pools are also present in the cerebellar and neocortical PCH2a organoids generated in this study, it remains elusive how they translate to the reduced size in PCH2a organoids resembling the clinical phenotype of affected individuals. Interestingly, in different model systems, tRNAs can directly regulate apoptosis (Avcilar-Kucukgoze and Kashina, 2020; Mei et al., 2010). Apoptosis has been suggested to occur in the cerebellum of affected individuals with PCH based on neuropathological observations in infants, children and adults (Barth et al., 2007) as well as in animal models of PCH (Kasher et al., 2011; Schmidt et al., 2022). We therefore investigated whether elevated apoptosis in our cerebellar and neocortical PCH2a organoids may explain the observed size differences (Fig. 5). At the very early time points of differentiation when neural progenitor cells are the dominant cell population, which were the focus of this study, we did not find any differences in apoptosis between PCH2a and control cerebellar and neocortical organoids (Fig. 5). It is possible that at later stages of differentiation, as neurons mature, apoptosis occurs, recapitulating human pathology. Future work addressing apoptosis rates in later stages of cerebellar organoid differentiation, which have recently been optimized and shown to generate more mature neuronal populations such as functional PCs (Atamian et al., 2024; Chen et al., 2023), will be informative to answer this question.

Alternatively, altered tRNA pools could directly affect differentiation. Specific tRNAs can change cell state and regulate proliferation and differentiation in concert with mRNAs (Gingold et al., 2014). Interestingly, in cancer, specific tRNAs can even promote metastatic progression (Goodarzi et al., 2016). We therefore hypothesize that the developing cerebellum and, to a lesser extent, the developing neocortex have specific requirements for appropriate tRNA pools throughout differentiation (Gao et al., 2024), originating perhaps from the increased neuronal output (Haldipur et al., 2022; Miller et al., 2019). It has been suggested that TSEN is required for processing cerebellum-specific pre-tRNAs (Sekulovski et al., 2021). Indeed, tRNA isodecoders display tissue-specific expression (Ishimura et al., 2014; Pinkard et al., 2020) and tRNA modifications change as oligodendrocyte precursor cells differentiate into oligodendrocytes (Martin et al., 2022), indicating that tRNA pools may be important regulators of neural lineage progression.

In this study, cerebellar organoids showed altered proliferation, indicated by an increased thickness and number of SOX2$^+$ rosettes, area of SOX2$^+$ rosettes over total organoid area (Fig. 6A-D), and percentage of Ki67$^+$/SOX2$^+$ dividing NPCs (Fig. 6E-H). Moreover, the direction of the changes in NPC proliferation was reversed from D30 to D50 of differentiation: PCH2a cerebellar organoids at D30 of differentiation appeared to consist largely of proliferative SOX2$^+$ cells, whereas they lost the majority of SOX2$^+$ area by D50. Such a change is seemingly counterintuitive to the smaller size of the PCH2a cerebellar organoids compared to that of control organoids over the course of differentiation. Although this phenomenon may be explained through an altered balance between proliferation and differentiation in the cerebellar organoids, the exact mechanism cannot be identified conclusively from our current study. Further in-depth analysis of our organoid model using, for instance, single-cell transcriptomics, as recently demonstrated on control cerebellar organoids (Atamian et al., 2024; Nayler et al., 2021), will reveal cellular and molecular differences between PCH2a and control organoids to explain the differences in size.

Based on our findings of altered proliferation in cerebellar organoids, we hypothesize that impaired proliferation and differentiation in the cerebellum leads to hypoplasia. Supporting this hypothesis, it has been reported that a different form of cerebellar hypoplasia (PCH17), caused by bi-allelic variants in *PRDM13* (OMIM *6167441 and #619909), comes with early disruption of cerebellar and brain stem development (Coolen et al., 2022). These neuropathological findings were supported by loss-of-function experiments in zebrafish, which revealed disruption of PC differentiation (Coolen et al., 2022). Moreover, altered development in several brain structures has been reported in human brain samples of a subtype of PCH (Patel et al., 2006). However, elucidating the exact mechanism of how defective TSEN54 function results in the clinical phenotypes of cerebellar hypoplasia and progressive microcephaly requires further mechanistic studies, and should ultimately be confirmed with pathological specimen and 3D reconstruction of magnetic resonance images of human brains at different developmental stages.

Regionalized neural organoid models for neurogenetic disorders

Human brain organoid models have been used extensively to study neurogenetic disorders in a human cellular context (Khakipoor et al., 2020; Velasco et al., 2020). In most cases, cerebral organoid models have been used, even when the cerebellum was primarily affected by the disorder (Bras et al., 2022), as cerebellar differentiation protocols have been developed only recently (Atamian et al., 2024; Chen et al., 2023; Hua et al., 2022; Muguruma et al., 2015; Nayler et al., 2021; Silva et al., 2020). Therefore, to date, the use of cerebellar organoids in neurogenetic disease modeling has not been demonstrated. For the first time in this study, we show how cerebellar organoids can be used to model the brain region-specific neuropathology of PCH2a, a severe neurological disorder that primarily affects the cerebellum, pons and, to a lesser extent, the neocortex. PCH2a iPSCs robustly differentiated into both the neocortical and cerebellar fate (Figs 4 and 5), in line with the observation that regional specification was not affected in a *tsen54* loss-of-function zebrafish (Kasher et al., 2011). Moreover, evidence for different cerebellar cell types including PCs and GCs were found in pathological studies of PCH2a (Rudnik-Schöneborn et al., 2014), indicating functional neural tube regionalization. However, we observed brain region-specific differences in organoid growth and proliferation between PCH2a and control organoids. We therefore suggest that using 3D differentiation protocols that replicate regional identity of the affected brain region is crucial to study a specific neuropathology. Consequently, if a disease affects multiple brain regions, the full potential of organoid technology may only be leveraged by combining different brain region-specific organoids.

MATERIALS AND METHODS

Recruitment of affected individuals

Affected individuals were recruited within our PCH2 natural history study, collecting clinical and diagnostic data, including diagnostic magnetic resonance images. Written informed consent was obtained from guardians and archived. All procedures were performed in accordance with the Helsinki Declaration. Individual-level data were deidentified. The study was approved by the ethics committee of the medical faculty, the local Institutional Review Boards of the Medical Faculty of the University of Tübingen, Germany (961/2020BO2 and 598/2011BO1), and Freiburg, Germany (20-1040).

Diagnostic confirmation by genetic sequencing

Next-generation sequencing and/or Sanger sequencing was performed after obtaining written informed consent for either clinical sequencing and/or center-specific institutional review board-approved research sequencing. All affected individuals harbored the hypomorphic founder variant c.919G>T in *TSEN54* in the homozygous state. The bi-allelic localization was confirmed by carrier testing.

Skin biopsies

Skin biopsies were acquired at different ages (9 months to 15 years) according to local standards of routine diagnostic procedures.

Culturing and reprogramming fibroblasts

Human dermal fibroblasts were obtained from skin biopsies and cultivated in Dulbecco's modified eagle medium (DMEM; Thermo Fisher Scientific) supplemented with 10% fetal bovine serum (FBS; Thermo Fisher Scientific) (fibroblast medium).

iPSC generation from fibroblasts was performed according to a published protocol with minor modifications (Okita et al., 2013). Briefly, reprogramming was initiated by nucleofection of 1×10^5 fibroblast with 1 µg of each episomal plasmid [pCXLE-hUL (Addgene #27080), pCXLE-hSK (Addgene #27078) and pCXLE-hOCT4 (Addgene #27076)] using the Nucleofector 2b transfection device (Lonza). Initially, fibroblasts were cultivated in fibroblast medium supplemented with 2 ng/ml FGF2 (Peprotech, 100-18B). On D3, the medium was changed to Essential 8 (E8) medium [DMEM/F12 (Thermo Fisher Scientific, 31330095), 64 mg/l L-ascorbic acid 2-phosphate magnesium (Sigma-Aldrich, A8960), 1% insulin-transferrin-selenium-supplement (100×) (Thermo Fisher Scientific, 41400045), 10 ng/ml FGF2 (Peprotech, 100-18B), 2 ng/ml TGFβ1 (Peprotech, 100-21C) and 100 ng/ml heparin (Sigma-Aldrich, H3393)] containing 100 µM sodium butyrate (NaB; Sigma-Aldrich, B5887). After 3-4 weeks, with medium changes every other day, iPSC colonies were manually picked and further expanded in E8 medium, performing medium changes daily. After ≥5 passages, they were genomically and functionally characterized and frozen in E8 medium containing 40% KO-SR (Thermo Fisher Scientific, 10828-028), 10% DMSO (Sigma-Aldrich, D4540) and 1 µM Y-27632 (Selleck Chemicals, S1049). All iPSC lines used in this study (three control lines and three PCH2a lines) were characterized according to the scientific guidelines for Lab Resources (https://www.sciencedirect.com/journal/stem-cell-research/about/lab-resources#scientific-guidelines-for-lab-resources).

Genomic integrity analysis

In order to verify genomic integrity, DNA of iPSCs and fibroblasts was isolated with DNeasy Blood and Tissue Kit (QIAGEN) according to the manufacturer's guidelines. Whole-genome SNP genotyping (SNP array) was conducted using Infinium OmniExpressExome-8-BeadChip (Illumina) and GenomeStudio V2.0.3 (Illumina) for evaluation. Copy number analysis was performed using the CNVPartition plugin (Illumina). Early mosaicism states were evaluated by manual review of B allele frequency plots on a chromosomal level. Results can be found in Data S1.

Pluripotency assessment

To assess ALP expression or for immunocytochemical analysis, iPSCs were fixed with 4% paraformaldehyde (PFA; Morphisto, 11762) and either assessed for ALP expression or permeabilized with 0.1% Triton X-100 (Sigma-Aldrich, T8787), blocked with 5% FBS and stained overnight at 4°C with primary antibodies for immunocytochemical analysis (rabbit anti-OCT4, 1:100, Proteintech, 11263-1-AP; and mouse anti-TRA-1-81, 1:500, Millipore, MAB4381). Samples were visualized after staining with Alexa Fluor 488-conjugated secondary antibodies (goat anti-rabbit and goat anti-mouse IgGs, 1:1000, Invitrogen, A-11001 and A-11008) for 1 h at room temperature. Nuclei were counterstained with Hoechst 33342 (1:10,000, Invitrogen). Samples were embedded in ProLong Gold Antifade Reagent (Thermo Fisher Scientific, P36930) and imaged with AxioImager Z1 (Zeiss).

The differentiation capacity of iPSCs into cells of all three germ layers was determined by an embryonic body (EB)-based protocol. 1.2×10^6 iPSCs were seeded in AggreWell800 plates (STEMCELL Technologies) in EB medium consisting of DMEM/F-12 (Gibco, 31330095) supplemented with 20% Knockout Serum Replacement (Gibco, 10828028), 1% MEM non-essential-amino-acid solution (Sigma-Aldrich, M5550-100ML), 1% penicillin/streptomycin (Sigma-Aldrich, P0781), 1% GlutaMAX (Thermo Fisher Scientific, 35050038) and 50 µM β-mercaptoethanol. On D4, EBs were plated onto coverslips for further differentiation. Specific expression of the markers TUJ (mouse anti-TUJ, 1:1000, Sigma-Aldrich, T8660) and SMA (mouse anti-SMA, 1:100, Dako, M0851) was assessed after 10 days as described above. For endodermal induction of iPSCs, 2×10^5 cells were seeded onto coverslips and cultivated in endoderm induction medium consisting of RPMI1640 Advanced (Gibco, 12633012) supplemented with 1× B27 (Thermo Fisher Scientific, 17504044), 1% penicillin/streptomycin, 0.2% fetal calf serum (FCS; Gibco, A5256701), 2 µM CHIR-99021 (Tocris, 4423) and 50 ng/ml activin A (Peprotech, 120-14P). At D4 of differentiation, cells were stained for FOXA2 (rabbit anti-FOXA2, 1:300, Millipore, 07-633), following the fixation and immunocytochemistry protocol mentioned above.

Sanger sequencing

To ensure the correct genetic background of all iPSC lines and control, Sanger sequencing was performed. Genomic DNA was extracted using the DNA Isolate kit (BioCat, BIO-52066-BL). The region of interest was amplified using the Phusion High-Fidelity PCR Kit (New England Biolabs, E0553S). The PCR product was purified with QIAquick PCR Purification Kit (QIAGEN, 28104) and samples were sent to Eurofins for sequencing. The following primers were used: forward, 5′-AGAAACCCCAGGAGT-3′, and reverse, 5′-CTCAATCCATCCGAG-3′.

iPSC culture

iPSC lines derived from affected individuals and control lines were generated following the same protocol and cultured under standard conditions (37°C, 5% CO_2 and 100% humidity) in E8 Flex medium (Gibco, A2858501) on human embryonic stem cell-qualified growth factor-reduced Matrigel-coated (Corning, 354277) cell culture dishes (Greiner, 657160). Passaging was performed in colonies using Gentle Dissociation Reagent (STEMCELL Technologies, 07174) once the culture reached 80-90% confluency. The culture medium was supplemented with thiazovivin (Sigma-Aldrich, 420220) until the following day. All cell lines were tested for mycoplasma contamination regularly with the PCR Mycoplasma Detection Set (TaKaRa, 6601) and maintained until passage 20. The pluripotency for each cell line was confirmed with an antibody against OCT4 (rabbit, 1:500, Abcam, ab19857) before each differentiation.

Staining of iPSCs

In order to assess the pluripotency and proliferation of all iPSCs used in this study, three consecutive passages per cell line were cultured on coverslips, fixed and stained for OCT4 (rabbit, 1:500, Abcam, ab19857), Ki67 (rabbit, 1:400, Cell Signaling Technology, 9661S) and cCas3 (rabbit, 1:600, Merck, AB9260). The cells were fixed with 4% PFA in PBS (Roth, 1105.1) for 15 min and carefully washed twice with 1× PBS. Prior to staining, the cells were permeabilized with 0.5% Triton X-100 for 10 min at room temperature. After washing the cells with 1× PBS for 5 min, they were incubated in blocking buffer, consisting of 10% normal donkey serum (Abcam, ab7475) in PBS, for 1 h at room temperature. The primary antibodies were diluted in blocking buffer and administered to the coverslips overnight at 4°C. The cells were washed three times with 1× PBS for 5 min and incubated with the secondary antibodies in blocking buffer for 1 h at room temperature. After two washes with 1× PBS for 5 min, the cells were counterstained with DAPI (1:5000; Thermo Fisher Scientific, D1306) in PBS. Finally, the cells were washed once in 1× PBS and mounted on slides using ProLong Gold. For all cell lines and conditions, coverslips were imaged at 20× magnification.

EdU incorporation

To quantify iPSC proliferation, three passages per cell line were treated with 10 µM EdU (Thermo Fisher Scientific, C10338) 3-4 days after the last passage for 1 and 4 h. After the incubation with EdU, cells were fixed and click chemistry was performed as advised by the manufacturer. The EdU signal was labeled with the provided Alexa Fluor 555 dye. Nuclear staining was performed with DAPI. Coverslips were imaged at 20× magnification on a confocal microscope, keeping laser settings identical for all cell lines and conditions.

Quantification of immunohistochemistry and click chemistry on iPSCs

In order to quantify possible differences in the expression of markers for pluripotency, proliferation and apoptosis and in the number of cells positive for EdU, we stained and imaged respective samples in one experiment. All samples were imaged with the same laser intensity settings on a confocal microscope. Raw image files were further processed in FIJI (Schindelin et al., 2012). Here, we used the watershed algorithm on the DAPI channel to identify individual nuclei. These were then registered as ROIs and counted. To analyze the number of stained cells, thresholding the respective channel of interest was performed with identical parameters for each channel and all samples according to the negative staining control. ROIs demonstrating a signal for the channel of interest were then measured and counted. This allowed us to analyze the percentage of cells positive for the marker of interest within the total population of cells. Finally, statistical analysis and plotting were performed in GraphPad Prism.

Generation of cerebellar organoids

Cerebellar organoids were generated as previously described (Silva et al., 2020) with some alterations: 80-90% confluent iPSCs were dissociated into single cells using accutase (Merck, A6964) and ∼4500 cells were seeded per well of 96-well V-bottom low-adhesion plates (S-Bio, MS-9096VZ) in E8 Flex medium supplemented with 10 µM Y-27632 (Cayman Chemical, 10005583). Once the aggregates reached a diameter of 250 µm, the medium was changed to growth factor-free chemically defined medium, supplemented with 50 ng/ml FGF2 and 10 µM SB-431542 (Tocris, 1614). At D7 of differentiation, FGF2 and SB-431542 were reduced to 33.3 ng/ml and 6.67 µM, respectively. At D14, the medium was supplemented with 100 ng/ml FGF19 (PeproTech, 100-32). The medium was changed to neurobasal medium (Gibco, 21103049) at D21, supplemented with 300 ng/ml SDF-1 (PeproTech, 300-28A) from D28 to D34. From D35 onwards, the medium was changed to complete BrainPhys (STEMCELL Technologies, 5793), supplemented with 10 µg/ml BDNF (PeproTech, 450-02), 100 µg/ml GDNF (PeproTech, 450-10), 100 mg/ml dbcAMP (PeproTech, 1698950) and 250 mM ascorbic acid (Tocris, 4055).

Generation of cortical organoids

Cortical organoids were generated as previously described (Pasca et al., 2015) with only minor alterations. In brief, 80-90% confluent iPSCs were dissociated into single cells using accutase and ∼9000 cells were seeded per well of 96-well V-bottom low-adhesion plates in E8 Flex medium supplemented with 10 µM Y-27632 (Cayman Chemical, 10005583). The medium was changed to neural induction medium (Essential 6, Thermo Fisher Scientific, A151640), supplemented with 2.5 µM dorsomorphin (Tocris, 3093), 10 µM SB-431542 and 2.5 µM XAV-939 (Tocris, 3748) the next day. Neural induction medium was changed every other day and replaced with neural maintenance medium (NM) (Neurobasal-A, Gibco, 10888-022) containing 1× B27 supplement without Vitamin A (Thermo Fisher Scientific, 12587010), 1× GlutaMAX and 1× penicillin/streptomycin at D6. NM medium was supplemented with 20 ng/ml EGF (Merck, GF144) and 20 ng/ml FGF2 from D6 to D24 and with 20 ng/ml BDNF and 20 ng/ml NT-3 (PeproTech, 450-03) from D25 to D43. NM medium was changed every other day and not supplemented after D43.

Size measurements

To investigate the size of organoids, brightfield images of the organoids were taken at D0, D10, D20, D30, D50, D70 and D90 of differentiation with an EVOS cell imaging system (Thermo Fisher Scientific). These images were analyzed using a published macro (Ivanov et al., 2014) for FIJI (Schindelin et al., 2012). The data were further analyzed with Excel, and Graph Pad Prism was used to plot data.

Fixation, cryosections and immunohistochemistry

Organoids were fixed at the respective time points in 4% PFA in PBS for 45-60 min at room temperature (Lancaster and Knoblich, 2014). The organoids were washed three times for 15 min with 1× PBS and then incubated in 30% sucrose (Sigma-Aldrich, S7903) in PBS solution at 4°C until they sunk to the bottom of the dish. The organoids were embedded in a 1:1 v/v mixture of 30% sucrose in PBS and optimal cutting temperature (OCT) compound (Sakura, 4583) and sectioned on Superfrost Plus slides (R. Langenbrinck GmbH, 03-0060) with a cryostat at 20 µm (Leica). The slides were stored at −80°C.

For immunohistochemistry, slides were thawed for 15 min at room temperature and the embedding solution was rinsed off with PBS. Antigen retrieval was achieved by immersing the slides in 10 mM citric acid buffer (pH 6.0) and boiling for 20 min in a microwave. A hydrophobic pen (PAP pen, Abcam, ab2601) was used to circle the sections to prevent the blocking solution from spilling during incubation. Permeabilization and blocking were performed with 1% Triton X-100, 0.2% gelatin (Sigma-Aldrich, G1890) and 10% normal donkey serum in PBS for 1 h at room temperature. Primary antibodies were diluted in permeabilization and blocking solution and applied to the sections overnight at 4°C. Subsequently, the slides were rinsed with PBS three times for 15 min, then secondary antibodies were diluted in permeabilization and blocking solution and applied for 3 h at room temperature. Details of primary and secondary antibodies can be found in Tables S4 and S5. The sections were rinsed in PBS three times for 15 min and nuclei were stained with DAPI (1:5000) diluted in PBS for 4 min. The sections were then rinsed in PBS and mounted using ProLong Gold.

Quantification of SOX2$^+$ zones

To quantify SOX2$^+$ area within individual organoids, we stained and imaged respective samples in one experiment. The laser intensity of the confocal microscope was adjusted according to the negative staining control. All samples were imaged with the same laser intensity settings. Raw image files were further processed in FIJI (Schindelin et al., 2012). To analyze the area of SOX2– zones, these regions were manually selected and measured. For each organoid and timepoint, all SOX2$^+$ zones were quantified using the ‘measure’ tool in FIJI. The area of the SOX2$^+$ zones was then normalized to the total DAPI$^+$ area of the organoid. To measure the thickness of the SOX2$^+$ zones, the outer and inner circumference was measured and the difference was calculated by subtracting the radius of the inner circumference from the radius of the outer circumference. Finally, statistical analysis and plotting were performed in GraphPad Prism.

Quantification of cCas3 over SOX2 staining

To quantify cCas3$^+$ area within ROIs in individual organoids, we stained and imaged respective samples in one experiment. The laser intensity of the confocal microscope was adjusted according to the negative staining control. All samples were imaged with the same laser intensity settings. Raw image files were further processed in FIJI (Schindelin et al., 2012). To analyze the area of stained cells, thresholding for cCas3 and SOX2 channels was performed with identical parameters for each channel and all samples. First, the area of cCas3-positively stained regions was quantified using the ‘measure’ tool in FIJI. Then, the cCas3$^+$ area was normalized to the SOX2$^+$ area of the respective image. Finally, statistical analysis and plotting were performed in GraphPad Prism.

Quantification of Ki67$^+$ cells over SOX2$^+$ cells

To quantify Ki67$^+$/SOX2$^+$ cells within ROIs in individual organoids, we stained and imaged the respective samples in one experiment. The laser intensity of the confocal microscope was adjusted according to the negative staining control. All samples were imaged with the same laser intensity settings. Raw image files were further processed in FIJI (Schindelin et al., 2012). Thresholding was adjusted to the respective channel and, for each channel, identical parameters were used for all samples. Watershed algorithm was used on the thresholded SOX2 channel to identify ROIs. ROIs were saved in ROI manager and results and transferred to the thresholded Ki67 channel. The numbers of Ki67$^+$ cells within these ROIs were counted and saved in the results file (Fig. S5). The results were exported to Excel to calculate percentages, and statistical analysis and plotting were performed in GraphPad Prism.

Statistical analysis

Details of specific statistical comparisons are listed in the relevant figure legends. Two-tailed unpaired *t*-tests were performed without correction for multiple comparisons. An overview of the replicates is shown in Table S3. No formal comparison of variances was performed between experimental groups. No statistical methods were used to predetermine sample size.

Acknowledgements

We thank the affected individuals and their families for donating samples. We would like to thank PCH-Familie e.V. for their support, especially Julia Matilainen and Axel Lankenau, for the fruitful discussions. We thank Clemens Lumper, Elisabeth Gustafsson, Lea Fischer, Jasmin Treu, Maximilian Feige, Christina Kulka, Ezgi Atay, Felix Hildebrand, Melanie Kraft and Yvonne Schelling for technical support. We thank Nicolas Snaidero for support with confocal microscopy. We thank Javier Martinez, Stefan Weitzer and Hansjürgen Volkmer for critical feedback on the manuscript. We thank the German Research Foundation (DFG) for supporting the acquisition of the confocal microscope used to acquire images in this study (INST 37/1170-1 FUGG, project number 467868227).

Competing interests

The authors declare no competing or financial interests.

Author contributions

Conceptualization: S.M., I.K.-M., L.S.; Methodology: T.K., K.S., S.H.; Formal Analysis: T.K., K.S.; Investigation: T.K., K.S., Z.Y., K.B., S.H.; Resources: L.L., W.G.J., S.G., I.K.-M.; Writing - original draft: T.K., K.S., S.M.; Writing - review and editing: T.K., S.H., K.S., L.L., S.G., W.G.J., Z.Y., K.B., L.S., I.K.-M., S.M.; Visualization: T.K., S.H., L.L.; Supervision: S.M., L.S., I.K.-M.; Project administration: T.K., S.M.; Funding acquisition: T.K., S.M., L.S.

Funding

We are grateful for financial support from PCH-Familie e.V., the Hertie Foundation (Gemeinnützige Hertie-Stiftung), the Ministerium für Wissenschaft, Forschung und Kunst Baden-Württemberg state postgraduate fellowship (to K.S. and T.K.) and the Heidelberger Akademie der Wissenschaften (WIN Kolleg). L.S., S.G. and I.K.-M. are members of the European Reference Network for Rare Neurological Diseases (ERN-RND) – project ID 739510. This project has been made possible in part by grant number 2022-316727 from the Chan Zuckerberg Initiative DAF, an advised fund of Silicon Valley Community Foundation. Open Access funding provided by University of Tübingen. Deposited in PMC for immediate release.

Data availability

All relevant data can be found within the article and its supplementary information.

References

Albanese, A., Swaney, J. M., Yun, D. H., Evans, N. B., Antonucci, J. M., Velasco, S., Sohn, C. H., Arlotta, P., Gehrke, L. and Chung, K. (2020). Multiscale 3D phenotyping of human cerebral organoids. *Sci. Rep.* **10**, 21487. doi:10.1038/s41598-020-78130-7

Aldinger, K. A., Thomson, Z., Phelps, I. G., Haldipur, P., Deng, M., Timms, A. E., Hirano, M., Santpere, G., Roco, C., Rosenberg, A. B. et al. (2021). Spatial and cell type transcriptional landscape of human cerebellar development. *Nat. Neurosci.* **24**, 1163-1175. doi:10.1038/s41593-021-00872-y

Ammann-Schnell, L., Groeschel, S., Kehrer, C., Frolich, S. and Krageloh-Mann, I. (2021). The impact of severe rare chronic neurological disease in childhood on the quality of life of families-a study on MLD and PCH2. *Orphanet J. Rare Dis.* **16**, 211. doi:10.1186/s13023-021-01828-y

Atamian, A., Birtele, M., Hosseini, N., Nguyen, T., Seth, A., Del Dosso, A., Paul, S., Tedeschi, N., Taylor, R., Coba, M. P. et al. (2024). Human cerebellar organoids with functional Purkinje cells. *Cell Stem Cell* **31**, 39-51.e6. doi:10.1016/j.stem.2023.11.013

Avcilar-Kucukgoze, I. and Kashina, A. (2020). Hijacking tRNAs from translation: regulatory functions of tRNAs in mammalian cell physiology. *Front. Mol. Biosci.* **7**, 610617. doi:10.3389/fmolb.2020.610617

Ballabio, C., Anderle, M., Gianesello, M., Lago, C., Miele, E., Cardano, M., Aiello, G., Piazza, S., Caron, D., Gianno, F. et al. (2020). Modeling medulloblastoma in vivo and with human cerebellar organoids. *Nat. Commun.* **11**, 583. doi:10.1038/s41467-019-13989-3

Barth, P. G., Aronica, E., de Vries, L., Nikkels, P. G., Scheper, W., Hoozemans, J. J., Poll-The, B.-T. and Troost, D. (2007). Pontocerebellar hypoplasia type 2: a neuropathological update. *Acta Neuropathol.* **114**, 373-386. doi:10.1007/s00401-007-0263-0

Bras, J., Henriques, D., Moreira, R., Santana, M. M., Silva-Pedrosa, R., Adão, D., Braz, S., Álvaro, A. R., de Almeida, L. P. and Mendonça, L. S. (2022). Establishment and characterization of human pluripotent stem cells-derived brain organoids to model cerebellar diseases. *Sci. Rep.* **12**, 12513. doi:10.1038/s41598-022-16369-y

Budde, B. S., Namavar, Y., Barth, P. G., Poll-The, B. T., Nurnberg, G., Becker, C., van Ruissen, F., Weterman, M. A. J., Fluiter, K., T te Beek, E. et al. (2008). tRNA splicing endonuclease mutations cause pontocerebellar hypoplasia. *Nat. Genet.* **40**, 1113-1118. doi:10.1038/ng.204

Chan, P. P. and Lowe, T. M. (2009). GtRNAdb: a database of transfer RNA genes detected in genomic sequence. *Nucleic Acids Res.* **37**, D93-D97. doi:10.1093/nar/gkn787

Chen, Y., Bury, L., Chen, F., Aldinger, K. A., Miranda, H. C. and Wynshaw-Boris, A. (2023). Generation of advanced cerebellar organoids for neurogenesis and neuronal network development. *Hum. Mol. Genet.* **32**, 2832-2841. doi:10.1093/hmg/ddad110

Coolen, M., Altin, N., Rajamani, K., Pereira, E., Siquier-Pernet, K., Puig Lombardi, E., Moreno, N., Barcia, G., Yvert, M., Laquerrière, A. et al. (2022). Recessive PRDM13 mutations cause fatal perinatal brainstem dysfunction with cerebellar hypoplasia and disrupt Purkinje cell differentiation. *Am. J. Hum. Genet.* **109**, 909-927. doi:10.1016/j.ajhg.2022.03.010

Eichmüller, O. L. and Knoblich, J. A. (2022). Human cerebral organoids — a new tool for clinical neurology research. *Nat. Rev. Neurol.* **18**, 661-680. doi:10.1038/s41582-022-00723-9

Ekert, K., Groeschel, S., Sanchez-Albisua, I., Frolich, S., Dieckmann, A., Engel, C. and Krägeloh-Mann, I. (2016). Brain morphometry in pontocerebellar hypoplasia type 2. *Orphanet J. Rare Dis.* **11**, 100. doi:10.1186/s13023-016-0481-4

Ermakova, O., Orsini, T., Gambadoro, A., Chiani, F. and Tocchini-Valentini, G. P. (2018). Three-dimensional microCT imaging of murine embryonic development from immediate post-implantation to organogenesis: application for phenotyping analysis of early embryonic lethality in mutant animals. *Mamm. Genome* **29**, 245-259. doi:10.1007/s00335-017-9723-6

Fleck, J. S., Sanchis-Calleja, F., He, Z., Santel, M., Boyle, M. J., Camp, J. G. and Treutlein, B. (2021). Resolving organoid brain region identities by mapping single-cell genomic data to reference atlases. *Cell Stem Cell* **28**, 1148-59.e8. doi:10.1016/j.stem.2021.02.015

Gao, L., Behrens, A., Rodschinka, G., Forcelloni, S., Wani, S., Strasser, K. and Nedialkova, D. D. (2024). Selective gene expression maintains human tRNA anticodon pools during differentiation. *Nat. Cell Biol.* **26**, 100-112. doi:10.1038/s41556-023-01317-3

Geschwind, D. H. and Rakic, P. (2013). Cortical evolution: judge the brain by its cover. *Neuron* **80**, 633-647. doi:10.1016/j.neuron.2013.10.045

Gingold, H., Tehler, D., Christoffersen, N. R., Nielsen, M. M., Asmar, F., Kooistra, S. M., Christophersen, N. S., Christensen, L. L., Borre, M., Sørensen, K. D. et al. (2014). A dual program for translation regulation in cellular proliferation and differentiation. *Cell* **158**, 1281-1292. doi:10.1016/j.cell.2014.08.011

Goodarzi, H., Nguyen, H. C. B., Zhang, S., Dill, B. D., Molina, H. and Tavazoie, S. F. (2016). Modulated expression of specific tRNAs drives gene expression and cancer progression. *Cell* **165**, 1416-1427. doi:10.1016/j.cell.2016.05.046

Haldipur, P., Millen, K. J. and Aldinger, K. A. (2022). Human cerebellar development and transcriptomics: implications for neurodevelopmental disorders. *Annu. Rev. Neurosci.* **45**, 515-531. doi:10.1146/annurev-neuro-111020-091953

Hayne, C. K., Butay, K. J. U., Stewart, Z. D., Krahn, J. M., Perera, L., Williams, J. G., Petrovitch, R. M., Deterding, L. J., Matera, A. G., Borgnia, M. J. et al. (2023). Structural basis for pre-tRNA recognition and processing by the human tRNA splicing endonuclease complex. *Nat. Struct. Mol. Biol.* **30**, 824-833. doi:10.1038/s41594-023-00991-z

Herculano-Houzel, S. (2012). Neuronal scaling rules for primate brains: the primate advantage. *Prog. Brain Res.* **195**, 325-340. doi:10.1016/B978-0-444-53860-4.00015-5

Hua, T., Liu, C., Kiran, S., Gray, K., Jung, S., Meckes, D. G., Li, Y. and Sang, Q.-X. A. (2022). Phenotypic, metabolic, and biogenesis properties of human stem cell-derived cerebellar spheroids. *Sci. Rep.* **12**, 12880. doi:10.1038/s41598-022-16970-1

Ishimura, R., Nagy, G., Dotu, I., Zhou, H., Yang, X. L., Schimmel, P., Senju, S., Nishimura, Y., Chuang, J. H. and Ackerman, S. L. (2014). RNA function. Ribosome stalling induced by mutation of a CNS-specific tRNA causes neurodegeneration. *Science* **345**, 455-459. doi:10.1126/science.1249749

Ivanov, D. P., Parker, T. L., Walker, D. A., Alexander, C., Ashford, M. B., Gellert, P. R. and Garnett, M. C. (2014). Multiplexing spheroid volume, resazurin and acid phosphatase viability assays for high-throughput screening of tumour spheroids and stem cell neurospheres. *PLoS One* **9**, e103817. doi:10.1371/journal.pone.0103817

Kadoshima, T., Sakaguchi, H., Nakano, T., Soen, M., Ando, S., Eiraku, M. and Sasai, Y. (2013). Self-organization of axial polarity, inside-out layer pattern, and species-specific progenitor dynamics in human ES cell-derived neocortex. *Proc. Natl Acad. Sci. USA* **110**, 20284-20289. doi:10.1073/pnas.1315710110

Kamei, T., Tamada, A., Kimura, T., Kakizuka, A., Asai, A. and Muguruma, K. (2023). Survival and process outgrowth of human iPSC-derived cells expressing Purkinje cell markers in a mouse model for spinocerebellar degenerative disease. *Exp. Neurol.* **369**, 114511. doi:10.1016/j.expneurol.2023.114511

Kang, H. J., Kawasawa, Y. I., Cheng, F., Zhu, Y., Xu, X., Li, M., Sousa, A. M. M., Pletikos, M., Meyer, K. A., Sedmak, G. et al. (2011). Spatio-temporal transcriptome of the human brain. *Nature* **478**, 483-489. doi:10.1038/nature10523

Kasher, P. R., Namavar, Y., van Tijn, P., Fluiter, K., Sizarov, A., Kamermans, M., Grierson, A. J., Zivkovic, D. and Baas, F. (2011). Impairment of the tRNA-splicing endonuclease subunit 54 (tsen54) gene causes neurological abnormalities and larval death in zebrafish models of pontocerebellar hypoplasia. *Hum. Mol. Genet.* **20**, 1574-1584. doi:10.1093/hmg/ddr034

Khakipoor, S., Crouch, E. E. and Mayer, S. (2020). Human organoids to model the developing human neocortex in health and disease. *Brain Res.* **1742**, 146803. doi:10.1016/j.brainres.2020.146803

Korneck, M., Wiora, L., Schols, L. and Hauser, S. (2022). Generation of two SPAST knockout human induced pluripotent stem cell lines to create a model for hereditary spastic paraplegia type 4. *Stem Cell Res* **60**, 102741. doi:10.1016/j.scr.2022.102741

Lago, C., Gianesello, M., Santomaso, L., Leva, G., Ballabio, C., Anderle, M., Antonica, F. and Tiberi, L. (2023). Medulloblastoma and high-grade glioma organoids for drug screening, lineage tracing, co-culture and in vivo assay. *Nat. Protoc.* **18**, 2143-2180. doi:10.1038/s41596-023-00839-2

Lancaster, M. A. and Knoblich, J. A. (2014). Generation of cerebral organoids from human pluripotent stem cells. *Nat. Protoc.* **9**, 2329-2340. doi:10.1038/nprot.2014.158

Lee, J. R., Kim, Y. H., Park, S. J., Choe, S. H., Cho, H. M., Lee, S. R., Kim, S. U., Kim, J. S., Sim, B. W., Song, B. S. et al. (2016). Identification of alternative variants and insertion of the novel polymorphic AluYl17 in TSEN54 gene during primate evolution. *Int J Genomics* **2016**, 1679574. doi:10.1155/2016/1679574

Leto, K., Arancillo, M., Becker, E. B. E., Buffo, A., Chiang, C., Ding, B., Dobyns, W. B., Dusart, I., Haldipur, P., Hatten, M. E. et al. (2016). Consensus paper: cerebellar development. *Cerebellum* **15**, 789-828. doi:10.1007/s12311-015-0724-2

Limperopoulos, C., Chilingaryan, G., Sullivan, N., Guizard, N., Robertson, R. L. and du Plessis, A. J. (2014). Injury to the premature cerebellum: outcome is related to remote cortical development. *Cereb. Cortex* **24**, 728-736. doi:10.1093/cercor/bhs354

Marek, S., Siegel, J. S., Gordon, E. M., Raut, R. V., Gratton, C., Newbold, D. J., Ortega, M., Laumann, T. O., Adeyemo, B., Miller, D. B. et al. (2018). Spatial and temporal organization of the individual human cerebellum. *Neuron* **100**, 977-93.e7. doi:10.1016/j.neuron.2018.10.010

Martin, S., Allan, K. C., Pinkard, O., Sweet, T., Tesar, P. J. and Coller, J. (2022). Oligodendrocyte differentiation alters tRNA modifications and codon optimality-mediated mRNA decay. *Nat. Commun.* **13**, 5003. doi:10.1038/s41467-022-32766-3

Mei, Y., Yong, J., Liu, H., Shi, Y., Meinkoth, J., Dreyfuss, G. and Yang, X. (2010). tRNA binds to cytochrome c and inhibits caspase activation. *Mol. Cell* **37**, 668-678. doi:10.1016/j.molcel.2010.01.023

Miller, D. J., Bhaduri, A., Sestan, N. and Kriegstein, A. (2019). Shared and derived features of cellular diversity in the human cerebral cortex. *Curr. Opin. Neurobiol.* **56**, 117-124. doi:10.1016/j.conb.2018.12.005

Mizuhara, E., Minaki, Y., Nakatani, T., Kumai, M., Inoue, T., Muguruma, K., Sasai, Y. and Ono, Y. (2010). Purkinje cells originate from cerebellar ventricular zone progenitors positive for Neph3 and E-cadherin. *Dev. Biol.* **338**, 202-214. doi:10.1016/j.ydbio.2009.11.032

Morales, D. and Hatten, M. E. (2006). Molecular markers of neuronal progenitors in the embryonic cerebellar anlage. *J. Neurosci.* **26**, 12226-12236. doi:10.1523/JNEUROSCI.3493-06.2006

Muguruma, K., Nishiyama, A., Kawakami, H., Hashimoto, K. and Sasai, Y. (2015). Self-organization of polarized cerebellar tissue in 3D culture of human pluripotent stem cells. *Cell Rep* **10**, 537-550. doi:10.1016/j.celrep.2014.12.051

Namavar, Y., Barth, P. G., Kasher, P. R., van Ruissen, F., Brockmann, K., Bernert, G., Writzl, K., Ventura, K., Cheng, E. Y., Ferriero, D. M. et al. (2011). Clinical, neuroradiological and genetic findings in pontocerebellar hypoplasia. *Brain* **134**, 143-156. doi:10.1093/brain/awq287

Nayler, S., Agarwal, D., Curion, F., Bowden, R. and Becker, E. B. E. (2021). High-resolution transcriptional landscape of xeno-free human induced pluripotent stem cell-derived cerebellar organoids. *Sci. Rep.* **11**, 12959. doi:10.1038/s41598-021-91846-4

Nowakowski, T. J., Bhaduri, A., Pollen, A. A., Alvarado, B., Mostajo-Radji, M. A., Di Lullo, E., Haeussler, M., Sandoval-Espinosa, C., Liu, S. J., Velmeshev, D. et al. (2017). Spatiotemporal gene expression trajectories reveal developmental hierarchies of the human cortex. *Science* **358**, 1318-1323. doi:10.1126/science.aap8809

Okita, K., Yamakawa, T., Matsumura, Y., Sato, Y., Amano, N., Watanabe, A., Goshima, N. and Yamanaka, S. (2013). An efficient nonviral method to generate integration-free human-induced pluripotent stem cells from cord blood and peripheral blood cells. *Stem Cells* **31**, 458-466. doi:10.1002/stem.1293

Pagliaro, A., Finger, R., Zoutendijk, I., Bunschuh, S., Clevers, H., Hendriks, D. and Artegiani, B. (2023). Temporal morphogen gradient-driven neural induction shapes single expanded neuroepithelium brain organoids with enhanced cortical identity. *Nat. Commun.* **14**, 7361. doi:10.1038/s41467-023-43141-1

Pasca, A. M., Sloan, S. A., Clarke, L. E., Tian, Y., Makinson, C. D., Huber, N., Kim, C. H., Park, J.-Y., O'Rourke, N. A., Nguyen, K. D. et al. (2015). Functional cortical neurons and astrocytes from human pluripotent stem cells in 3D culture. *Nat. Methods* **12**, 671-678. doi:10.1038/nmeth.3415

Pasca, S. P., Arlotta, P., Bateup, H. S., Camp, J. G., Cappello, S., Gage, F. H., Knoblich, J. A., Kriegstein, A. R., Lancaster, M. A., Ming, G.-L. et al. (2022). A nomenclature consensus for nervous system organoids and assembloids. *Nature* **609**, 907-910. doi:10.1038/s41586-022-05219-6

Patel, M. S., Becker, L. E., Toi, A., Armstrong, D. L. and Chitayat, D. (2006). Severe, fetal-onset form of olivopontocerebellar hypoplasia in three sibs: PCH type 5? *Am. J. Med. Genet. A* **140**, 594-603. doi:10.1002/ajmg.a.31095

Pinkard, O., McFarland, S., Sweet, T. and Coller, J. (2020). Quantitative tRNA-sequencing uncovers metazoan tissue-specific tRNA regulation. *Nat. Commun.* **11**, 4104. doi:10.1038/s41467-020-17879-x

Rudnik-Schöneborn, S., Barth, P. G. and Zerres, K. (2014). Pontocerebellar hypoplasia. *Am. J. Med. Genet. C Semin. Med. Genet.* **166**, 173-183. doi:10.1002/ajmg.c.31403

Sanchez-Albisua, I., Frolich, S., Barth, P. G., Steinlin, M. and Krageloh-Mann, I. (2014). Natural course of pontocerebellar hypoplasia type 2A. *Orphanet J. Rare Dis.* **9**, 70. doi:10.1186/1750-1172-9-70

Sarieva, K. and Mayer, S. (2021). The effects of environmental adversities on human neocortical neurogenesis modeled in brain organoids. *Front. Mol. Biosci.* **8**, 686410. doi:10.3389/fmolb.2021.686410

Schaffer, A. E., Pinkard, O. and Coller, J. M. (2019). tRNA Metabolism and Neurodevelopmental Disorders. *Annu. Rev. Genomics Hum. Genet.* **20**, 359-387. doi:10.1146/annurev-genom-083118-015334

Schindelin, J., Arganda-Carreras, I., Frise, E., Kaynig, V., Longair, M., Pietzsch, T., Preibisch, S., Rueden, C., Saalfeld, S., Schmid, B. et al. (2012). Fiji: an open-source platform for biological-image analysis. *Nat. Methods* **9**, 676-682. doi:10.1038/nmeth.2019

Schmidt, C. A., Min, L. Y., McVay, M. H., Giusto, J. D., Brown, J. C., Salzler, H. R. and Matera, A. G. (2022). Mutations in Drosophila tRNA processing factors cause phenotypes similar to Pontocerebellar Hypoplasia. *Biol. Open* **11**, bio058928. doi:10.1242/bio.058928

Sekulovski, S., Devant, P., Panizza, S., Gogakos, T., Pitiriciu, A., Heitmeier, K., Ramsay, E. P., Barth, M., Schmidt, C., Tuschl, T. et al. (2021). Assembly defects of human tRNA splicing endonuclease contribute to impaired pre-tRNA processing in pontocerebellar hypoplasia. *Nat. Commun.* **12**, 5610. doi:10.1038/s41467-021-25870-3

Sekulovski, S., Susac, L., Stelzl, L. S., Tampe, R. and Trowitzsch, S. (2023). Structural basis of substrate recognition by human tRNA splicing endonuclease TSEN. *Nat. Struct. Mol. Biol.* **30**, 834-840. doi:10.1038/s41594-023-00992-y

Silva, T. P., Fernandes, T. G., Nogueira, D. E. S., Rodrigues, C. A. V., Bekman, E. P., Hashimura, Y., Jung, S., Lee, B., Carmo-Fonseca, M. and Cabral, J. M. S. (2020). Scalable generation of mature cerebellar organoids from human pluripotent stem cells and characterization by immunostaining. *J Vis Exp.* **160**, e61143. doi:10.3791/61143

Sloan, S. A., Andersen, J., Pasca, A. M., Birey, F. and Pasca, S. P. (2018). Generation and assembly of human brain region-specific three-dimensional cultures. *Nat. Protoc.* **13**, 2062-2085. doi:10.1038/s41596-018-0032-7

Stork, T., Nessler, J., Anderegg, L., Hunerfauth, E., Schmutz, I., Jagannathan, V., Kyöstilä, K., Lohi, H., Baumgärtner, W., Tipold, A. et al. (2019). TSEN54 missense variant in Standard Schnauzers with leukodystrophy. *PLoS Genet.* **15**, e1008411. doi:10.1371/journal.pgen.1008411

Trotta, C. R., Paushkin, S. V., Patel, M., Li, H. and Peltz, S. W. (2006). Cleavage of pre-tRNAs by the splicing endonuclease requires a composite active site. *Nature* **441**, 375-377. doi:10.1038/nature04741

Uhlen, M., Fagerberg, L., Hallstrom, B. M., Lindskog, C., Oksvold, P., Mardinoglu, A., Sivertsson, Å., Kampf, C., Sjöstedt, E., Asplund, A. et al. (2015). Proteomics. Tissue-based map of the human proteome. *Science* **347**, 1260419. doi:10.1126/science.1260419

van Dijk, T., Baas, F., Barth, P. G. and Poll-The, B. T. (2018). What's new in pontocerebellar hypoplasia? An update on genes and subtypes. *Orphanet J. Rare Dis.* **13**, 92. doi:10.1186/s13023-018-0826-2

Velasco, S., Paulsen, B. and Arlotta, P. (2020). 3D Brain organoids: studying brain development and disease outside the embryo. *Annu. Rev. Neurosci.* **43**, 375-389. doi:10.1146/annurev-neuro-070918-050154

Volpato, V. and Webber, C. (2020). Addressing variability in iPSC-derived models of human disease: guidelines to promote reproducibility. *Dis. Model. Mech.* **13**, dmm042317. doi:10.1242/dmm.042317

Wang, B., Harrison, W., Overbeek, P. A. and Zheng, H. (2011). Transposon mutagenesis with coat color genotyping identifies an essential role for Skor2 in sonic hedgehog signaling and cerebellum development. *Development* **138**, 4487-4497. doi:10.1242/dev.067264

Yuan, L., Han, Y., Zhao, J., Zhang, Y. and Sun, Y. (2023). Recognition and cleavage mechanism of intron-containing pre-tRNA by human TSEN endonuclease complex. *Nat. Commun.* **14**, 6071. doi:10.1038/s41467-023-41845-y

Zhang, Z., O'Laughlin, R., Song, H. and Ming, G. L. (2022). Patterning of brain organoids derived from human pluripotent stem cells. *Curr. Opin. Neurobiol.* **74**, 102536. doi:10.1016/j.conb.2022.102536

Zhang, X., Yang, F., Zhan, X., Bian, T., Xing, Z., Lu, Y. and Shi, Y. (2023). Structural basis of pre-tRNA intron removal by human tRNA splicing endonuclease. *Mol. Cell* **83**, 1328-39.e4. doi:10.1016/j.molcel.2023.03.015

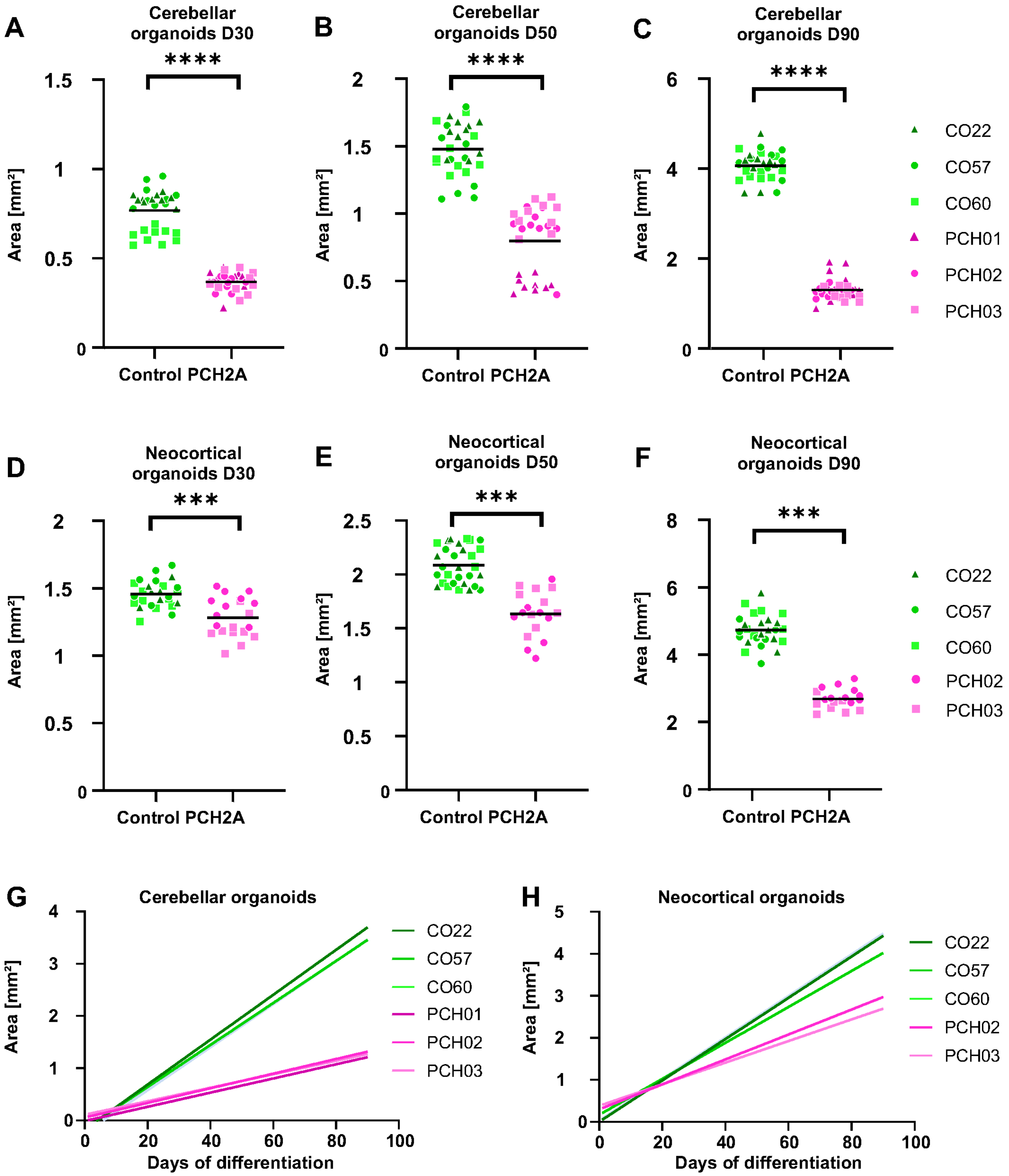

Fig. S1. Size differences of cerebellar and neocortical organoids at different stages of differentiation. Quantification of the area of cerebellar (A-C) and neocortical (D-F) control and PCH2a organoid areas at D30, D50 and D90 of differentiation. Sizes of organoids differ significantly between PCH2a and control organoids. (****, $p < 0.0001$, *** $p < 0.001$ unpaired t-test with Welch's correction assuming unequal SDs). n>8 organoids per cell line, time point and differentiation. (G) Linear regression model for growth curves of cerebellar organoids. (H) Linear regression model for growth curves of neocortical organoids.

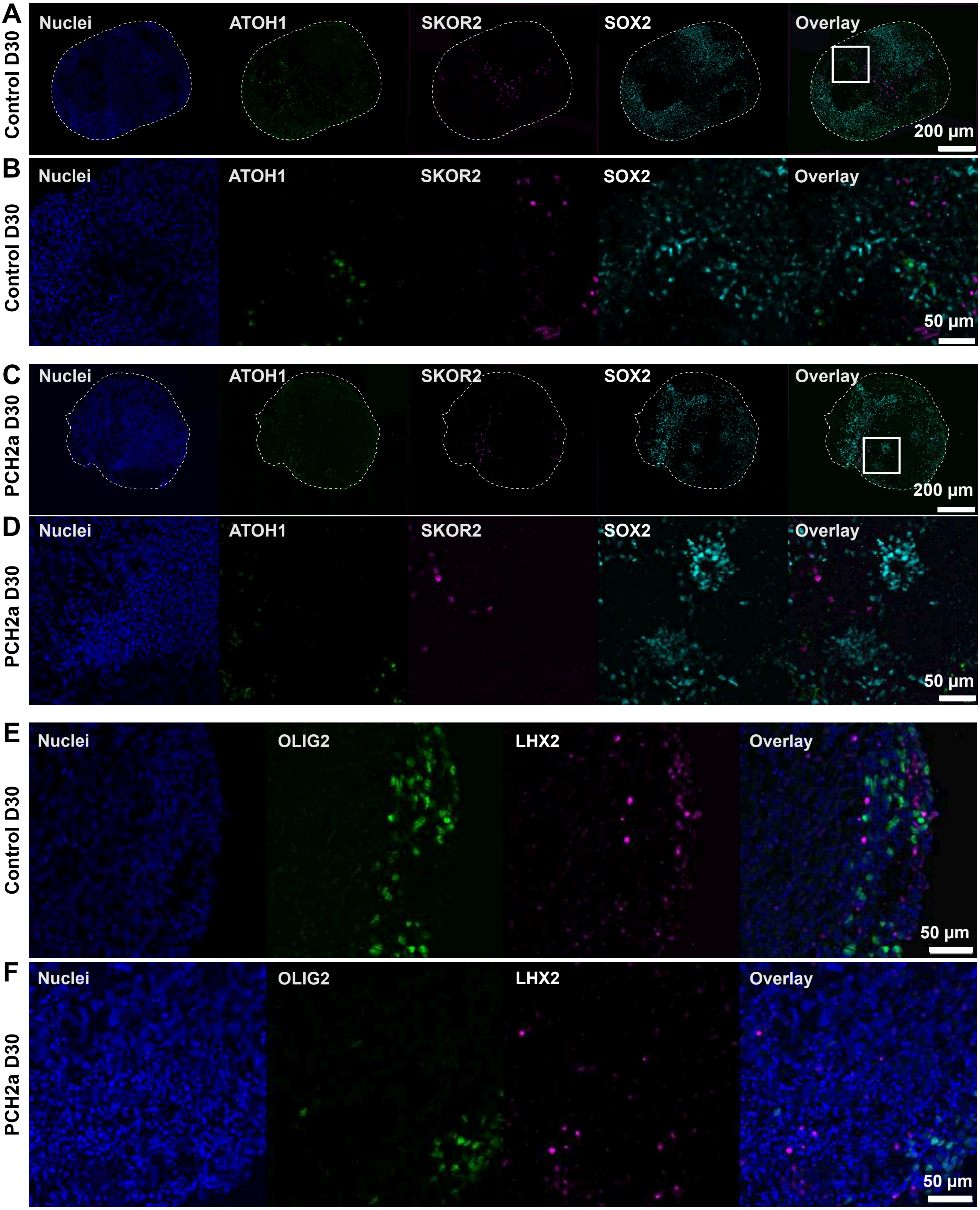
A
Control D30
Nuclei
ATOH1
SKOR2
SOX2
Overlay
200 µm
B
Control D30
Nuclei
ATOH1
SKOR2
SOX2
Overlay
50 µm
C
PCH2a D30
Nuclei
ATOH1
SKOR2
SOX2
Overlay
200 µm
D
PCH2a D30
Nuclei
ATOH1
SKOR2
SOX2
Overlay
50 µm
E
Control D30
Nuclei
OLIG2
LHX2
Overlay
50 µm
F
PCH2a D30
Nuclei
OLIG2
LHX2
Overlay
50 µm

Fig. S2. PCH2a and control cerebellar organoids show differentiation into cerebellar lineage. (A-D) ATOH1 (green) expression demonstrates the presence of rhombic lip derived granule cell precursors while SKOR2 (magenta) is marker for young Purkinje cells derived from the cerebellar VZ, both markers are present in control (A, B) and PCH2a (C, D) cerebellar organoids (representative images CO57 P18, PCH03 P19). Dotted lines indicate the outline of organoids, white squares (A,C) indicate the region of the zoom-in (B, D). (E, F) Staining for early Purkinje marker OLIG2 (green) and LHX2 (magenta), early marker for nuclear transitory zone cells in Day 30 control (E) and PCH2a (F) cerebellar organoids (representative images CO60 P19, PCH01 P19). Nuclei are stained with DAPI.

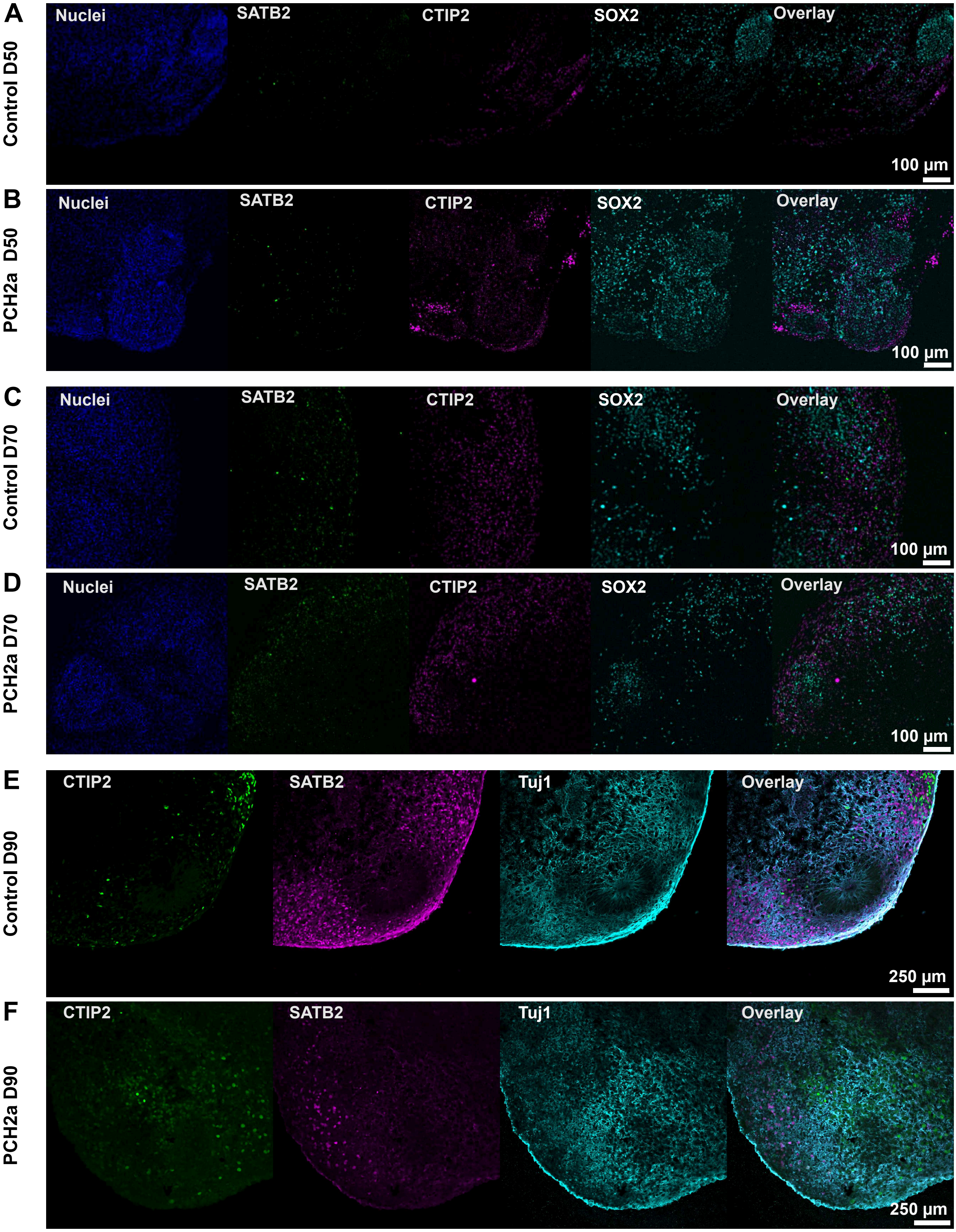
A
Control D50
Nuclei
SATB2
CTIP2
SOX2
Overlay
100 µm
B
PCH2a D50
Nuclei
SATB2
CTIP2
SOX2
Overlay
100 µm
C
Control D70
Nuclei
SATB2
CTIP2
SOX2
Overlay
100 µm
D
PCH2a D70
Nuclei
SATB2
CTIP2
SOX2
Overlay
100 µm
E
Control D90
CTIP2
SATB2
Tuj1
Overlay
250 µm
F
PCH2a D90
CTIP2
SATB2
Tuj1
Overlay
250 µm

Fig. S3. PCH2a and control neocortical organoids express layer-specific neuronal markers. (A-F) Epifluorescent microscopy images of immunohistochemistry on neocortical organoid sections. Control (A) and PCH2a (B) neocortical organoids express early-born deep-layer neuronal marker CTIP2 (magenta) at D50 of differentiation (representative images CO22 P19, PCH03 P19). (C, D, E, F) Control (C) and PCH2a (D) neocortical organoids show expression of CTIP2 as well upper layer neuronal marker SATB2 (green) at D70 (C, D) (representative images CO22 P19, PCH02 P17) and D90 (E, F) (representative images CO57 P18, PCH03 P19) of differentiation (CTIP2 green, SATB2 magenta). Nuclei are stained with DAPI.

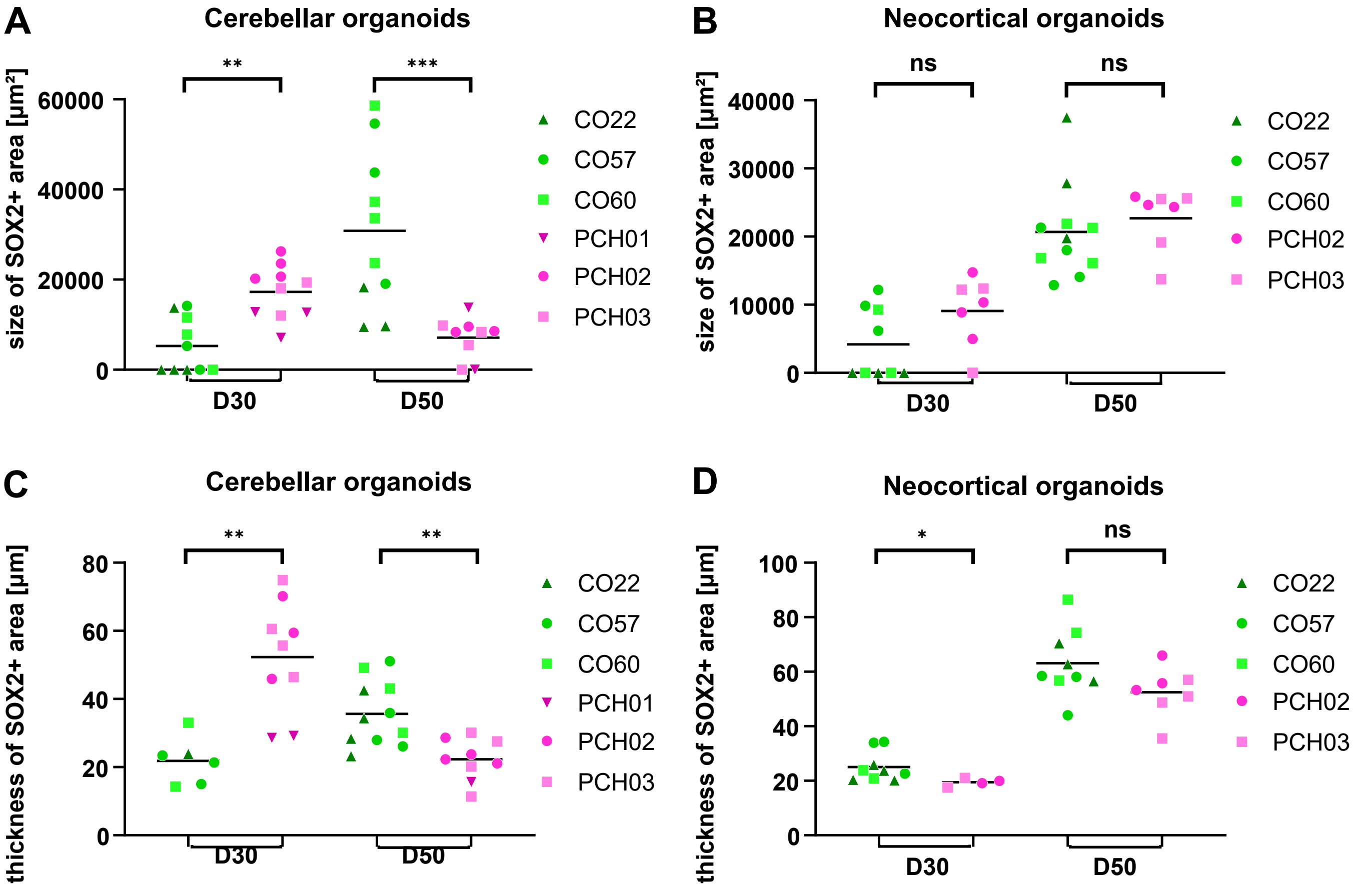

Fig. S4. Morphology of SOX2+ structures differs in PCH2a and control organoids. (A) SOX2+ structures are significantly bigger in PCH2a organoids at D30 of differentiation. At D50 control organoids show significantly bigger SOX2+ structures. (B) SOX2+ structures do not show difference in size at D30 and D50 of differentiation in neocortical organoids. (C) PCH2a cerebellar organoids show thicker SOX2+ structures at D30 of differentiation while SOX2+ structures are thicker in control organoids at D50. (D) Thickness of SOX2+ structures is lower in PCH2a neocortical organoids at D30 of differentiation. There is no difference in thickness of these structures at D50 of differentiation in neocortical organoids ($p>0.05$ for ns and $p<0.05$ for *, $p<0.01$ for**, $p<0.001$ for ***unpaired t-test with Welch's correction assuming unequal SDs).

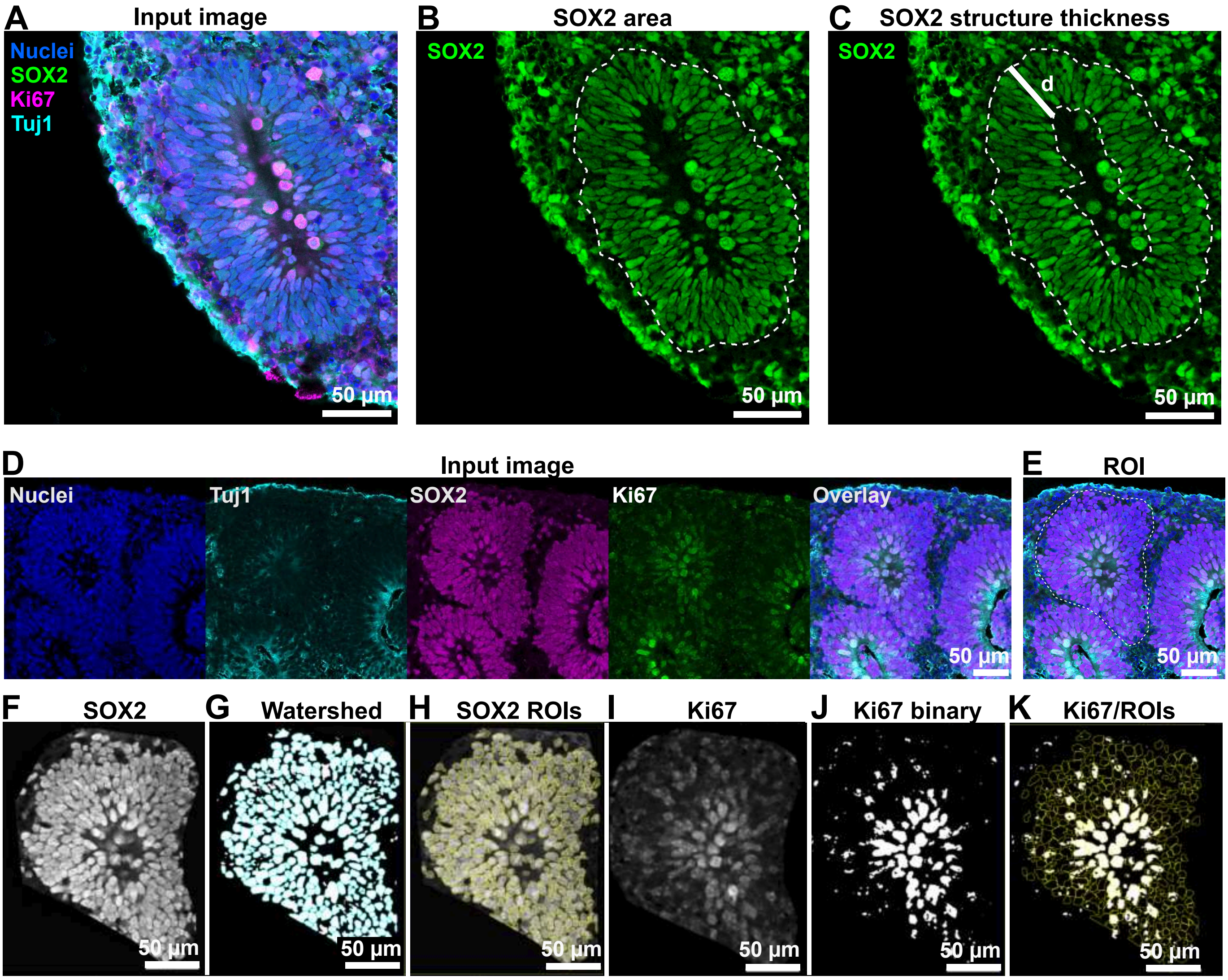

Fig. S5. Overview of methods for image analysis for SOX2+ rosettes. (A) Overlay of input image for size and thickness analysis of SOX2+ rosettes. (B) SOX2 channel of input image. White dotted line indicates outline of rosette used for size analysis of rosette structures. (C) SOX2 channel of input image. Outer dotted line indicates outline of SOX2+ rosette, while inner dotted structures indicates boarder to lumen. Thickness (d) of SOX2+ rosettes was calculated by subtracting the inner border from the circumference resulting in the mean thickness of the whole rosette structure. Images in A-C show a PCH2a cerebellar organoid at D30 of differentiation also shown in Fig. 6E. (D) Individual channels and overlay of input image for quantification of Ki67+/SOX2+ cells. (E) White dotted lines indicate region of interest (ROI) for quantification of Ki67+/SOX2+ cells. (F) Input SOX2 channel. (G) Watershed algorithm on thresholded SOX2 image. (H) Overlay of ROIs resulting from watershed algorithm on input image. (I) Ki67 input image. (J) Thresholded Ki67 image. (K) Overlay of SOX2 ROIs on thresholded Ki67 image. All SOX2 ROIs with Ki67 signal were counted as Ki67+/SOX2+ cells. Nuclei are stained with DAPI.

Table S1. Clinical features of PCH2a probands.

Table S2. Linear regression model of regionalized neural organoid growth.

Table S3. Overview of experimental replicates.

Table S4. Primary Antibodies

Antibody	species	vendor	cat number	batch number	dilution
ATOH1	mouse	Merck	WH0000474M1	J8071-1B12	1:500
BAHRL1	rabbit	Atlas Antibodies	HPA004809	7306	1:500
Calbindin	mouse	Merck	C9848	125953	1:500
cCas3	rabbit	CST	9661S	47	1:400
CTIP2	rat	Abcam	ab18465	OR3427932,2	1:500
Ki67	rabbit	Merck	AB9260	41423360	1:600
Kirrel2	rabbit	Atlas Antibodies	HPA071587	R101296	1:500
LHX2	goat	Merck	SAB2500593	8573P1	1:500
Map2	rabbit	Abcam	ab32454	GR3453941-2	1:500
OCT4	rabbit	Abcam	ab19857	GR3284176-1	1:500
Olig2	rabbit	Merck	AB9610	3857662	1:500
SATB2	rabbit	Abcam	ab34735	GR3262034-2	1:500
SKOR2	rabbit	Atlas Antibodies	HPA046206	B96020	1:500
SOX2	goat	R&D Systems	AF2018	KOY0622061	1:500
TSEN54	rabbit	Invitrogen	PA5-101939	WL34558767	1:500
Tuj1	mouse	Atlas Antibodies	AMAb91394	3024	1:500

Table S5. Secondary antibodies

Host species	Target species	Fluorophore	Provider	Cat.no
donkey	goat	AF555	Abcam	ab150130
donkey	goat	AF647	Abcam	A21447
donkey	mouse	AF568	Abcam	ab175472
donkey	mouse	AF647	Abcam	A31571
donkey	rabbit	AF488	Abcam	A21206
donkey	rabbit	AF546	Abcam	A10040
donkey	rabbit	AF647	Abcam	A31573
donkey	sheep	AF488	Abcam	A11015
donkey	sheep	AF647	Abcam	A21448

Data S1. Karyotype reports of generated iPSCs.

Available for download at
https://journals.biologists.com/dmm/article-lookup/doi/10.1242/dmm.050740#supplementary-data

Karyotype Report

Customer sample ID: iPS-CO-22_2.1
Internal sample ID: DE04SCRHIHD100022
Date of receipt: 2020-02-26

Gender
Stated: Unknown
Chr. X derived: Male

Genotype identity with: DESCRHIH00023

Karyotyping

Technology used: Illumina BeadArray

Product: HumanOmni2.5Exome-8 BeadChip v1.4
Manifest file: HumanOmni2-5Exome-8v1-4_A1.bpm
Cluster file: HumanOmni2-5Exome-8v1-4_A1.egt

Chip barcode and segment: 203730650093 R02C01

Batch ID and 96 well position: WG6911135-MSA6 B05

Call rate: 0,9976248

Typing
Scanner: Illumina iScan, S/N: N263
Site of processing: Life&Brain GENOMICS, Bonn, Germany
Manufacturer: Illumina, Inc., San Diego, United States of America
Date of scan: 2020-03-31-1456

Genotype Analysis
Genome Studio: GenomeStudio V2.0.4
Genotyping module: Ver. 2.0.4

Copy Number Analysis
Algorithm applied: CNV-Partition
Version: 3.2.0
Software producer: Illumina, Inc., San Diego, United States of America

Noteworthy findings

No larger chromosomal aberrations to be reported.

Control Dashboard

Sample_ID / Sentrix_Label	Category	Control (BeadType)	Section 1 X	Section 1 Y	State
DESCRHIH00022 / 203730650093_R02C01	Staining	DNP (High) (27630314)	20239	110	OK/OK
DESCRHIH00022 / 203730650093_R02C01	Staining	DNP (Bgnd) (29619375)	261	211	OK/OK
DESCRHIH00022 / 203730650093_R02C01	Staining	Biotin (High) (41666334)	287	9696	OK/OK
DESCRHIH00022 / 203730650093_R02C01	Staining	Biotin (Bgnd) (34648333)	220	84	OK/OK
DESCRHIH00022 / 203730650093_R02C01	Extension	Extension (A) (17616306)	17544	294	Notable/OK
DESCRHIH00022 / 203730650093_R02C01	Extension	Extension (T) (14607337)	19510	257	Notable/OK
DESCRHIH00022 / 203730650093_R02C01	Extension	Extension (C) (12613307)	731	10601	OK/OK
DESCRHIH00022 / 203730650093_R02C01	Extension	Extension (G) (11603365)	821	9764	OK/Notable
DESCRHIH00022 / 203730650093_R02C01	Target Removal	Target Removal (31623323)	486	206	OK/OK
DESCRHIH00022 / 203730650093_R02C01	Hybridization	Hyb (High) (19612319)	1167	10813	OK/Notable
DESCRHIH00022 / 203730650093_R02C01	Hybridization	Hyb (Medium) (20636378)	349	6851	OK/OK
DESCRHIH00022 / 203730650093_R02C01	Hybridization	Hyb (Low) (23617335)	982	2204	OK/OK
DESCRHIH00022 / 203730650093_R02C01	Stringency	String (PM) (32629312)	12362	284	Notable/OK
DESCRHIH00022 / 203730650093_R02C01	Stringency	String (MM) (33668307)	2315	182	OK/OK
DESCRHIH00022 / 203730650093_R02C01	Non-Specific Binding	NSB (Bgnd) (26619332)	240	190	OK/OK
DESCRHIH00022 / 203730650093_R02C01	Non-Specific Binding	NSB (Bgnd) (27624356)	223	186	OK/OK
DESCRHIH00022 / 203730650093_R02C01	Non-Specific Binding	NSB (Bgnd) (25617343)	241	192	OK/OK
DESCRHIH00022 / 203730650093_R02C01	Non-Specific Binding	NSB (Bgnd) (24616350)	264	190	OK/OK
DESCRHIH00022 / 203730650093_R02C01	Non-Polymorphic	NP (A) (34633358)	6289	247	OK/OK
DESCRHIH00022 / 203730650093_R02C01	Non-Polymorphic	NP (T) (16648324)	8394	246	OK/OK
DESCRHIH00022 / 203730650093_R02C01	Non-Polymorphic	NP (C) (43641328)	448	5688	OK/Notable
DESCRHIH00022 / 203730650093_R02C01	Non-Polymorphic	NP (G) (13642359)	472	5285	OK/Notable
DESCRHIH00022 / 203730650093_R02C01	Restoration	Restore (28637363)	273	212	OK/OK

All „Notable“ tagged probes are within specs. The karyogram can be evaluated.

Karyogram

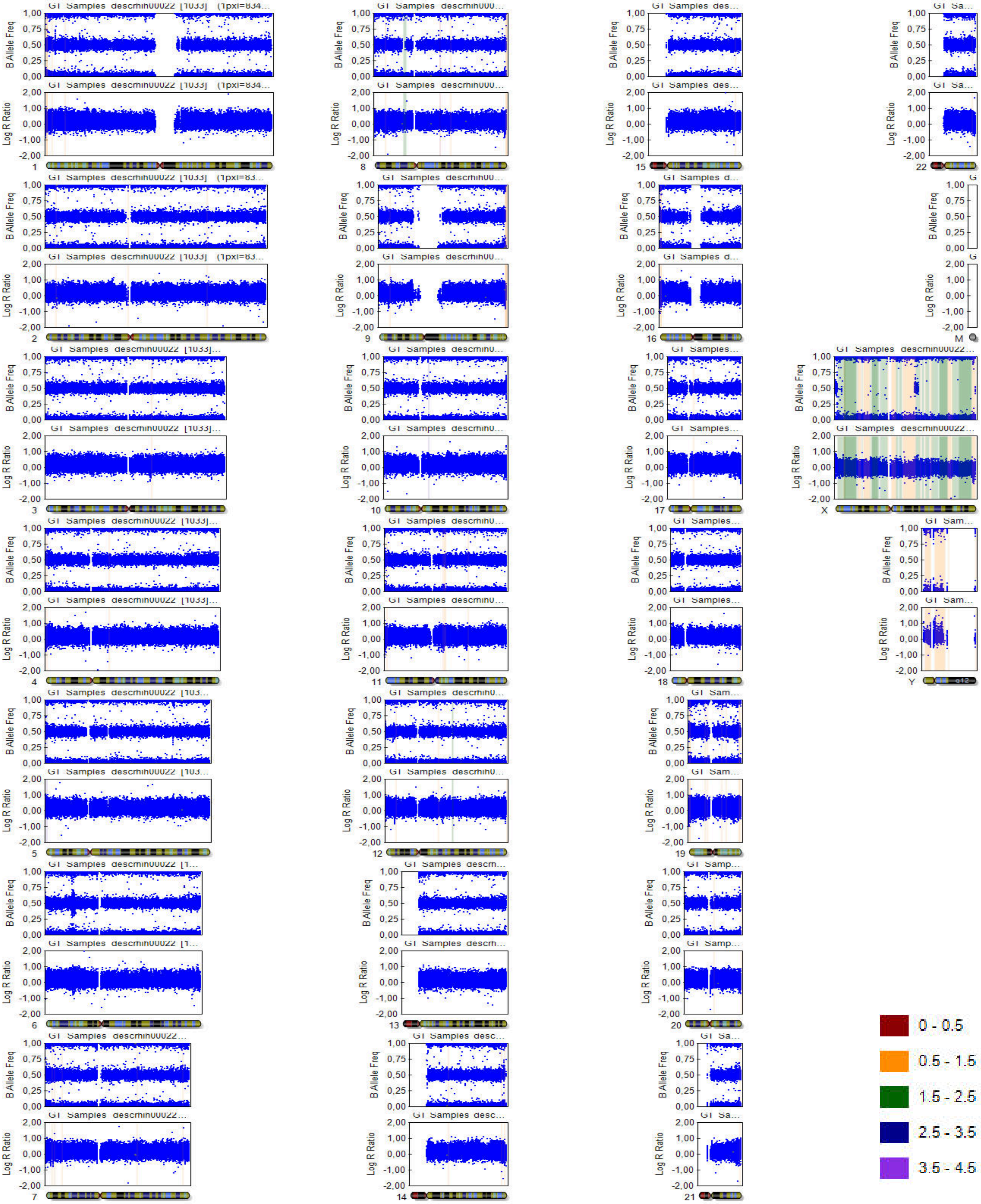
B Allele Freq
Log R Ratio
1,00
0,75
0,50
0,25
0,00
2,00
1,00
0,00
-1,00
-2,00
1
2
3
4
5
6
7
8
9
10
11
12
13
14
15
16
17
18
19
20
21
22
X
Y
M
0 - 0.5
0.5 - 1.5
1.5 - 2.5
2.5 - 3.5
3.5 - 4.5

Copy Number Analysis

Copy number events will be reported if larger than 350'000 base pairs, 1Mbp for loss of heterozygosity regions.
Database of Genomic Variants comparison: Number stated represent population based copy number variants that span the reported event completely.

Copy number analysis
Algorithm applied: CNV-Partition
Version: 3.2
Software producer: Illumina, Inc., San Diego, United States of America

Sample ID	**Chr**	**Start**	**End**	**Type**	**Length**	**Marker count**	**CN Confidence**	**DGV Comparison**
DESCRHIH00022	8	31781189	35324420	2	3543231	2334	455,1505	
DESCRHIH00022	12	72825139	74758965	2	1933826	1162	235,608	

Karyotype Report

Customer sample ID:27_iPS-CO-57cl.B.1
Internal sample ID: DE86SCRDZND100143
Date of receipt: 26.07.2018

Gender
Stated: Unknown
Chr. X derived: Male

Genotype identity with: 28_F-CO-57-2018-07-26 / DESCRDZN00144

Karyotyping

Technology used: Illumina BeadArray

Product: HumanOmni2.5Exome-8 BeadChip v1.3
Manifest file: HumanOmni2-5Exome-8v1-3_A1.bpm
Cluster file: HumanOmni2-5Exome-8v1-3_A1.egt

Chip barcode and segment: 201364830139 R03C01

Batch ID and 96 well position: WG6906661-MSA6 C04

Call rate: 0,9981163

Typing
Scanner: Illumina iScan, S/N: N234
Site of processing: Life&Brain GENOMICS, Bonn, Germany
Manufacturer: Illumina, Inc., San Diego, United States of America
Date of scan: 2018-08-01-2310

Genotype Analysis
Genome Studio: GenomeStudio V2.0.2
Genotyping module: Ver. 2.0.2

Copy Number Analysis
Algorithm applied: CNV-Partition
Version: 3.2
Software producer: Illumina, Inc., San Diego, United States of America

Noteworthy findings

No larger chromosomal aberrations to be reported.

Control Dashboard

Sample_ID / Sentrix_Label	Category	Control (BeadType)	Section 1 X	Section 1 Y	State
DESCRDZN00143 / 201364830139_R03C01	Staining	DNP (High) (27630314)	27305	137	OK/OK
DESCRDZN00143 / 201364830139_R03C01	Staining	DNP (Bgnd) (29619375)	387	223	OK/OK
DESCRDZN00143 / 201364830139_R03C01	Staining	Biotin (High) (41666334)	486	12740	OK/OK
DESCRDZN00143 / 201364830139_R03C01	Staining	Biotin (Bgnd) (34648333)	374	100	OK/OK
DESCRDZN00143 / 201364830139_R03C01	Extension	Extension (A) (17616306)	27672	396	OK/OK
DESCRDZN00143 / 201364830139_R03C01	Extension	Extension (T) (14607337)	30291	315	OK/OK
DESCRDZN00143 / 201364830139_R03C01	Extension	Extension (C) (12613307)	1063	13549	OK/OK
DESCRDZN00143 / 201364830139_R03C01	Extension	Extension (G) (11603365)	1345	13010	OK/OK
DESCRDZN00143 / 201364830139_R03C01	Target Removal	Target Removal (31623323)	677	179	OK/OK
DESCRDZN00143 / 201364830139_R03C01	Hybridization	Hyb (High) (19612319)	1329	12828	OK/OK
DESCRDZN00143 / 201364830139_R03C01	Hybridization	Hyb (Medium) (20636378)	550	7772	OK/OK
DESCRDZN00143 / 201364830139_R03C01	Hybridization	Hyb (Low) (23617335)	1251	2588	OK/OK
DESCRDZN00143 / 201364830139_R03C01	Stringency	String (PM) (32629312)	17938	361	OK/OK
DESCRDZN00143 / 201364830139_R03C01	Stringency	String (MM) (33668307)	4743	270	OK/OK
DESCRDZN00143 / 201364830139_R03C01	Non-Specific Binding	NSB (Bgnd) (26619332)	365	166	OK/OK
DESCRDZN00143 / 201364830139_R03C01	Non-Specific Binding	NSB (Bgnd) (27624356)	350	164	OK/OK
DESCRDZN00143 / 201364830139_R03C01	Non-Specific Binding	NSB (Bgnd) (25617343)	347	185	OK/OK
DESCRDZN00143 / 201364830139_R03C01	Non-Specific Binding	NSB (Bgnd) (24616350)	380	156	OK/OK
DESCRDZN00143 / 201364830139_R03C01	Non-Polymorphic	NP (A) (34633358)	9101	296	OK/OK
DESCRDZN00143 / 201364830139_R03C01	Non-Polymorphic	NP (T) (16648324)	11388	240	OK/OK
DESCRDZN00143 / 201364830139_R03C01	Non-Polymorphic	NP (C) (43641328)	619	6573	OK/OK
DESCRDZN00143 / 201364830139_R03C01	Non-Polymorphic	NP (G) (13642359)	517	5944	OK/Notable
DESCRDZN00143 / 201364830139_R03C01	Restoration	Restore (28637363)	371	197	OK/OK

All „Notable“ tagged probes are within specs. The karyogram can be evaluated.

Karyogram

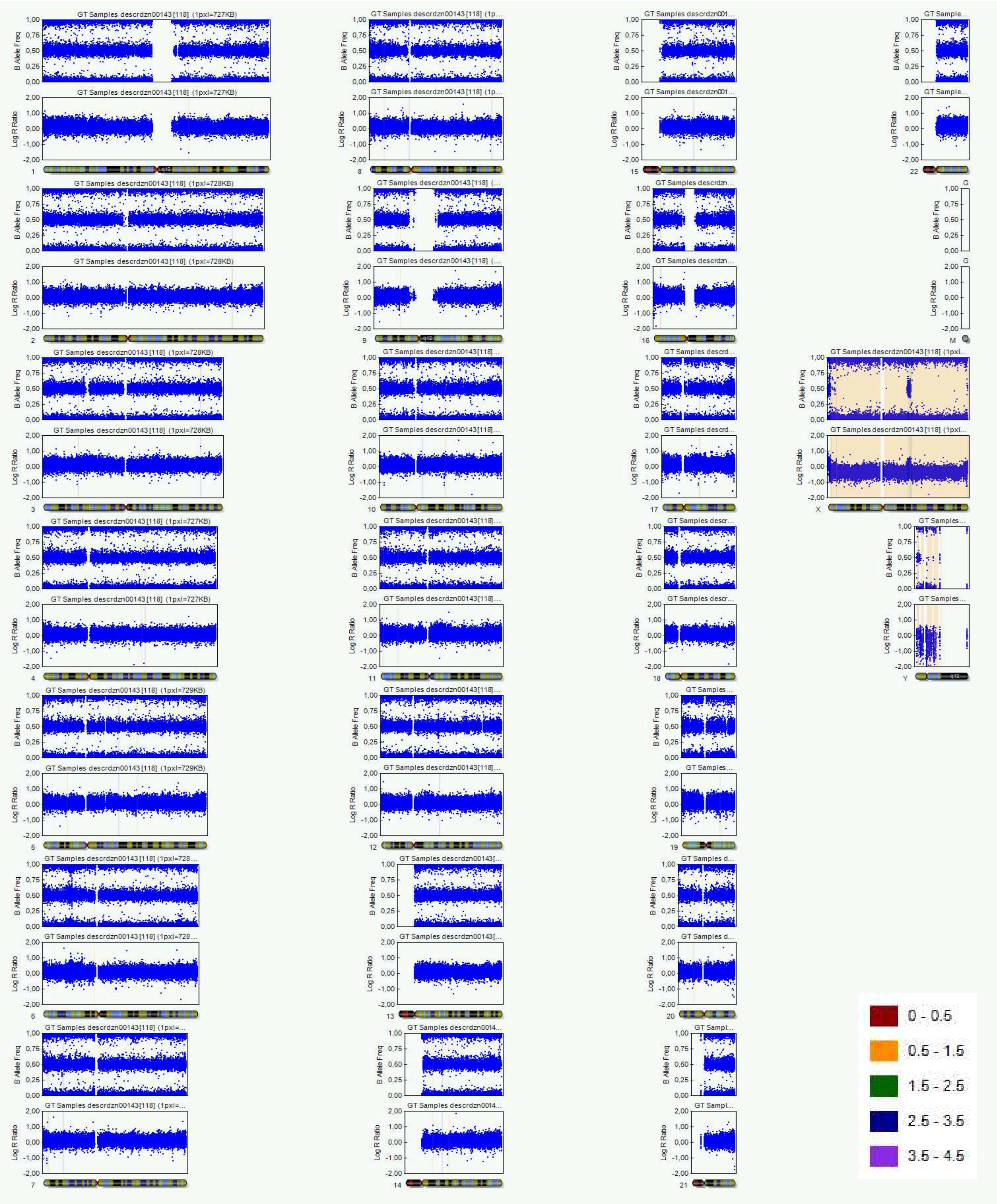
GT Samples descrdzn00143 [118] (1pxl=727KB)
B Allele Freq
Log R Ratio
1,00
0,75
0,50
0,25
0,00
2,00
1,00
0,00
-1,00
-2,00
1
2
3
4
5
6
7
8
9
10
11
12
13
14
15
16
17
18
19
20
21
22
G
M
X
Y
q12
0 - 0.5
0.5 - 1.5
1.5 - 2.5
2.5 - 3.5
3.5 - 4.5

Copy Number Analysis

Copy number events will be reported if larger than 350'000 base pairs, 1Mbp for loss of heterozygosity regions.
Database of Genomic Variants comparison: Number stated represent population based copy number variants that span the reported event completely.

Copy number analysis
Algorithm applied: CNV-Partition
Version: 3.2
Software producer: Illumina, Inc., San Diego, United States of America

Sample ID	Chr	Start	End	Type	Length	Marker count	CN Confidence	DGV Comparison
DESCRDZN00143	8	43057452	43806224	3	748772	361	427,1952	

Karyotype Report

Customer sample ID: iPS-CO-60_4.3
Internal sample ID: DE47SCRHIHD100024
Date of receipt: 2020-02-26

Gender
Stated: Unknown
Chr. X derived: Male

Genotype identity with: DESCRHIH00025

Karyotyping

Technology used: Illumina BeadArray

Product: HumanOmni2.5Exome-8 BeadChip v1.4
Manifest file: HumanOmni2-5Exome-8v1-4_A1.bpm
Cluster file: HumanOmni2-5Exome-8v1-4_A1.egt

Chip barcode and segment: 203730650093 R04C01

Batch ID and 96 well position: WG6911135-MSA6 D05

Call rate: 0,997606

Typing
Scanner: Illumina iScan, S/N: N263
Site of processing: Life&Brain GENOMICS, Bonn, Germany
Manufacturer: Illumina, Inc., San Diego, United States of America
Date of scan: 2020-03-31-1503

Genotype Analysis
Genome Studio: GenomeStudio V2.0.4
Genotyping module: Ver. 2.0.4

Copy Number Analysis
Algorithm applied: CNV-Partition
Version: 3.2.0
Software producer: Illumina, Inc., San Diego, United States of America

Noteworthy findings

No larger chromosomal aberrations to be reported.

Control Dashboard

Sample_ID / Sentrix_Label	Category	Control (BeadType)	Section 1 X	Section 1 Y	State
DESCRHIH00024 / 203730650093_R04C01	Staining	DNP (High) (27630314)	21958	137	OK/OK
DESCRHIH00024 / 203730650093_R04C01	Staining	DNP (Bgnd) (29619375)	344	203	OK/OK
DESCRHIH00024 / 203730650093_R04C01	Staining	Biotin (High) (41666334)	321	12082	OK/OK
DESCRHIH00024 / 203730650093_R04C01	Staining	Biotin (Bgnd) (34648333)	247	110	OK/OK
DESCRHIH00024 / 203730650093_R04C01	Extension	Extension (A) (17616306)	20971	373	OK/OK
DESCRHIH00024 / 203730650093_R04C01	Extension	Extension (T) (14607337)	23411	283	OK/OK
DESCRHIH00024 / 203730650093_R04C01	Extension	Extension (C) (12613307)	878	12869	OK/OK
DESCRHIH00024 / 203730650093_R04C01	Extension	Extension (G) (11603365)	959	12222	OK/OK
DESCRHIH00024 / 203730650093_R04C01	Target Removal	Target Removal (31623323)	598	252	OK/OK
DESCRHIH00024 / 203730650093_R04C01	Hybridization	Hyb (High) (19612319)	1366	13100	OK/OK
DESCRHIH00024 / 203730650093_R04C01	Hybridization	Hyb (Medium) (20636378)	384	8349	OK/OK
DESCRHIH00024 / 203730650093_R04C01	Hybridization	Hyb (Low) (23617335)	1176	2737	OK/OK
DESCRHIH00024 / 203730650093_R04C01	Stringency	String (PM) (32629312)	14996	379	OK/OK
DESCRHIH00024 / 203730650093_R04C01	Stringency	String (MM) (33668307)	3141	269	OK/OK
DESCRHIH00024 / 203730650093_R04C01	Non-Specific Binding	NSB (Bgnd) (26619332)	313	201	OK/OK
DESCRHIH00024 / 203730650093_R04C01	Non-Specific Binding	NSB (Bgnd) (27624356)	324	197	OK/OK
DESCRHIH00024 / 203730650093_R04C01	Non-Specific Binding	NSB (Bgnd) (25617343)	299	228	OK/OK
DESCRHIH00024 / 203730650093_R04C01	Non-Specific Binding	NSB (Bgnd) (24616350)	296	226	OK/OK
DESCRHIH00024 / 203730650093_R04C01	Non-Polymorphic	NP (A) (34633358)	7804	266	OK/OK
DESCRHIH00024 / 203730650093_R04C01	Non-Polymorphic	NP (T) (16648324)	9916	297	OK/OK
DESCRHIH00024 / 203730650093_R04C01	Non-Polymorphic	NP (C) (43641328)	522	7149	OK/OK
DESCRHIH00024 / 203730650093_R04C01	Non-Polymorphic	NP (G) (13642359)	537	6188	OK/OK
DESCRHIH00024 / 203730650093_R04C01	Restoration	Restore (28637363)	363	206	OK/OK

All probes are within specs. The karyogram can be evaluated.

Karyogram

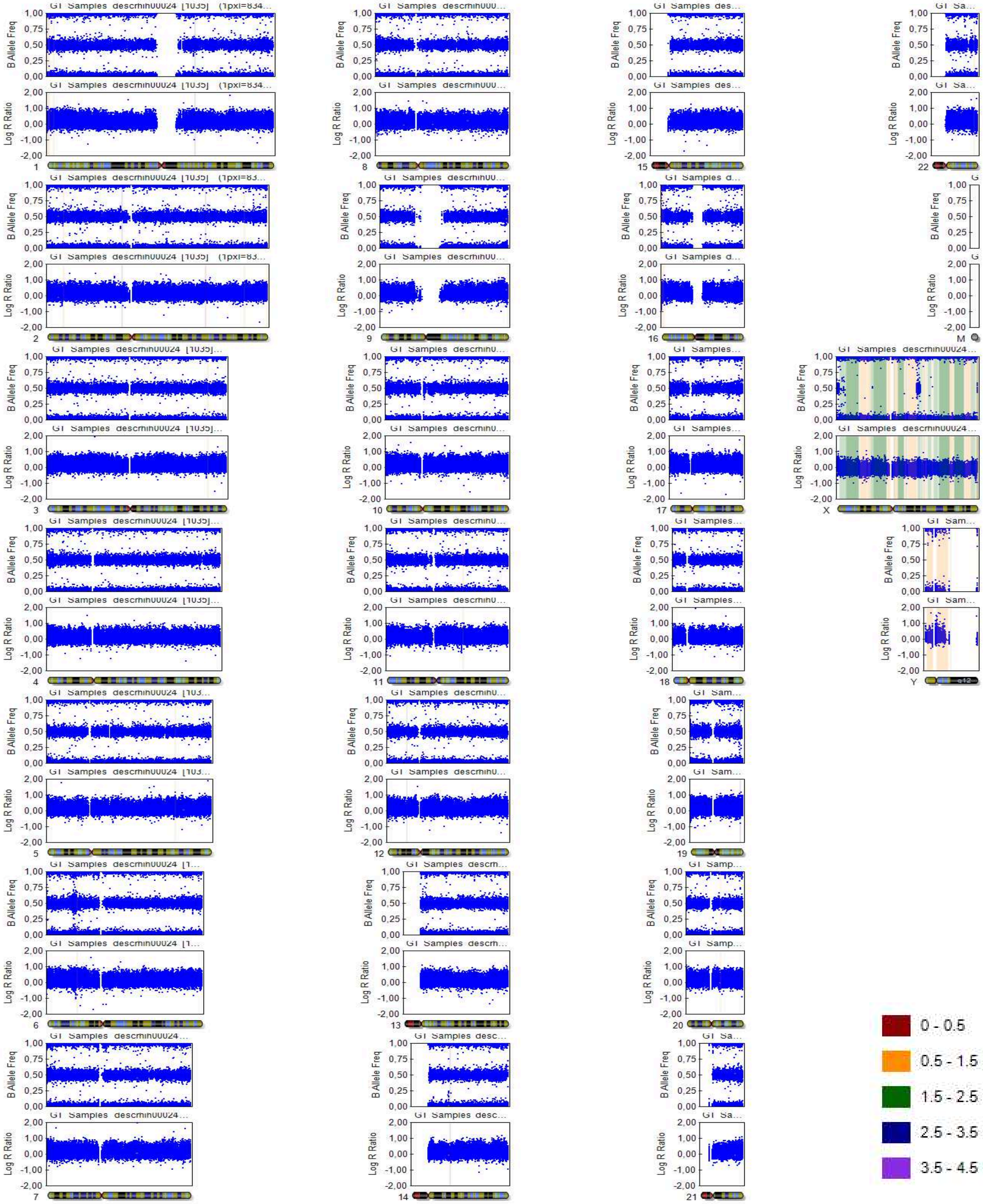
GT Samples descrhih00024 [1035]
B Allele Freq
1,00
0,75
0,50
0,25
0,00
Log R Ratio
2,00
1,00
0,00
-1,00
-2,00
1
2
3
4
5
6
7
8
9
10
11
12
13
14
15
16
17
18
19
20
21
22
M
X
Y
0 - 0.5
0.5 - 1.5
1.5 - 2.5
2.5 - 3.5
3.5 - 4.5

Copy Number Analysis

Copy number events will be reported if larger than 350'000 base pairs, 1Mbp for loss of heterozygosity regions.
Database of Genomic Variants comparison: Number stated represent population based copy number variants that span the reported event completely.

Copy number analysis
Algorithm applied: CNV-Partition
Version: 3.2
Software producer: Illumina, Inc., San Diego, United States of America

Sample ID	Chr	Start	End	Type	Length	Marker count	CN Confidence	DGV Comparison
DESCRHIH00024	12	20522796	21680693	2	1157897	1493	342,3974	
DESCRHIH00024	23	2700157	24993887	2	22293730	11958	1481,305	
DESCRHIH00024	23	25000842	33074340	1	8073498	4676	676,9131	
DESCRHIH00024	23	33112111	37029338	1	3917227	1767	289,3273	
DESCRHIH00024	23	37033484	54733713	2	17700229	7686	1490,719	
DESCRHIH00024	23	54736227	58563509	1	3827282	990	70,9988	
DESCRHIH00024	23	61686465	62573853	1	887388	185	146,1671	
DESCRHIH00024	23	63400883	67085251	1	3684368	976	271,2258	CNV-Gain: 1, OTHER-Inversion: 2
DESCRHIH00024	23	67097144	74027649	2	6930505	2957	2351,022	
DESCRHIH00024	23	74031648	76230687	1	2199039	618	66,9812	
DESCRHIH00024	23	76237943	77787620	2	1549677	293	678,5046	
DESCRHIH00024	23	77804801	88440097	1	10635296	4446	1318,529	
DESCRHIH00024	23	88442047	92374313	2	3932266	1160	248,2036	
DESCRHIH00024	23	92547980	94025957	2	1477977	831	1801,044	
DESCRHIH00024	23	94027807	95538643	1	1510836	738	313,9972	
DESCRHIH00024	23	95544051	97068109	2	1524058	763	1833,992	
DESCRHIH00024	23	97074770	99554768	1	2479998	903	165,7551	
DESCRHIH00024	23	99557421	104463794	2	4906373	1423	3124,86	

DESCRHIH00024	23	104464069	106109204	1	1645135	428	164,2652	
DESCRHIH00024	23	106112751	111616869	2	5504118	1301	963,7	
DESCRHIH00024	23	111650324	123584863	2	11934539	2763	1477,011	
DESCRHIH00024	23	123588245	128397152	1	4808907	897	251,0483	
DESCRHIH00024	23	128398819	140002446	2	11603627	2758	1564,544	
DESCRHIH00024	23	140010139	147122830	1	7112691	1731	612,3635	
DESCRHIH00024	23	147158718	152213311	2	5054593	1464	1059,053	
DESCRHIH00024	23	152222116	153282028	1	1059912	385	427,3397	
DESCRHIH00024	23	153698458	154916845	2	1218387	380	825,4448	CNV-Gain: 1, CNV-Gain+Loss: 1
DESCRHIH00024	24	2657176	10082095	1	7424919	728	3551,399	
DESCRHIH00024	24	13133499	24891486	1	11757987	1499	7184,58	

Karyotype Report

Customer sample ID: iPS-PCH-01_3.1_p11
Internal sample ID: DE34SCRDZND100206
Date of receipt: 2021-03-09

Gender
Stated: Unstated
Chr. X derived: Male

Genotype identity with: F-PCH-01_P3-2021-03-09 / DESCRDZN00202,
IPS-PCH-01_2.1_P11-2021-03-09 / DESCRDZN00205

Karyotyping

Technology used: Illumina BeadArray

Product: HumanOmni2.5Exome-8 BeadChip v1.5
Manifest file: InfiniumOmni2-5Exome-8v1-5_A1.bpm
Cluster file: InfiniumOmni2-5Exome-8v1-5_A1-Cluster-File.egt

Chip barcode and segment: 204372050103 R07C01

Batch ID and 96 well position: WG6917121-MSA6 G02

Call rate: 0,9986958

Typing
Scanner: Illumina iScan, S/N: N234
Site of processing: Life&Brain GENOMICS, Bonn, Germany
Manufacturer: Illumina, Inc., San Diego, United States of America
Date of scan: 2021-03-17-1200

Genotype Analysis
Genome Studio: GenomeStudio V2.0.5
Genotyping module: Ver. 2.0.5

Copy Number Analysis
Algorithm applied: CNV-Partition
Version: 3.2.0
Software producer: Illumina, Inc., San Diego, United States of America

Noteworthy findings

No larger chromosomal aberrations to be reported.

Control Dashboard

Sample_ID / Sentrix_Label	Category	Control (BeadType)	Section 1 X	Section 1 Y	State
DESCRDZN00206 / 204372050103_R07C01	Staining	DNP (High) (27630314)	37630	369	OK/OK
DESCRDZN00206 / 204372050103_R07C01	Staining	DNP (Bgnd) (43603326)	710	450	Notable/ Notable
DESCRDZN00206 / 204372050103_R07C01	Staining	Biotin (High) (41666334)	792	20828	OK/OK
DESCRDZN00206 / 204372050103_R07C01	Staining	Biotin (Bgnd) (34648333)	582	355	Notable/OK
DESCRDZN00206 / 204372050103_R07C01	Extension	Extension (A) (17616306)	36574	466	OK/OK
DESCRDZN00206 / 204372050103_R07C01	Extension	Extension (T) (14607337)	37520	410	OK/OK
DESCRDZN00206 / 204372050103_R07C01	Extension	Extension (C) (12613307)	1845	21676	OK/OK
DESCRDZN00206 / 204372050103_R07C01	Extension	Extension (G) (11603365)	2118	21803	Notable/OK
DESCRDZN00206 / 204372050103_R07C01	Target Removal	Target Removal (31623323)	1220	256	OK/OK
DESCRDZN00206 / 204372050103_R07C01	Hybridization	Hyb (High) (19612319)	1778	22924	OK/OK
DESCRDZN00206 / 204372050103_R07C01	Hybridization	Hyb (Medium) (20636378)	771	15775	OK/OK
DESCRDZN00206 / 204372050103_R07C01	Hybridization	Hyb (Low) (23617335)	1949	4464	OK/OK
DESCRDZN00206 / 204372050103_R07C01	Stringency	String (PM) (32629312)	26788	516	OK/OK
DESCRDZN00206 / 204372050103_R07C01	Stringency	String (MM) (33668307)	9148	380	Notable/OK
DESCRDZN00206 / 204372050103_R07C01	Non-Specific Binding	NSB (Bgnd) (28637363)	528	370	OK/OK
DESCRDZN00206 / 204372050103_R07C01	Non-Specific Binding	NSB (Bgnd) (27624356)	596	283	OK/OK
DESCRDZN00206 / 204372050103_R07C01	Non-Specific Binding	NSB (Bgnd) (25617343)	1828	287	OK/OK
DESCRDZN00206 / 204372050103_R07C01	Non-Specific Binding	NSB (Bgnd) (24616350)	558	1113	OK/OK
DESCRDZN00206 / 204372050103_R07C01	Non-Polymorphic	NP(A) (34633358)	13152	391	OK/OK
DESCRDZN00206 / 204372050103_R07C01	Non-Polymorphic	NP(T) (16648324)	19273	444	OK/OK
DESCRDZN00206 / 204372050103_R07C01	Non-Polymorphic	NP(C) (43641328)	901	11699	OK/OK
DESCRDZN00206 / 204372050103_R07C01	Non-Polymorphic	NP(G) (13642359)	932	11048	OK/OK

All „Notable“ tagged probes are within specs. The karyogram can be evaluated.

Karyogram

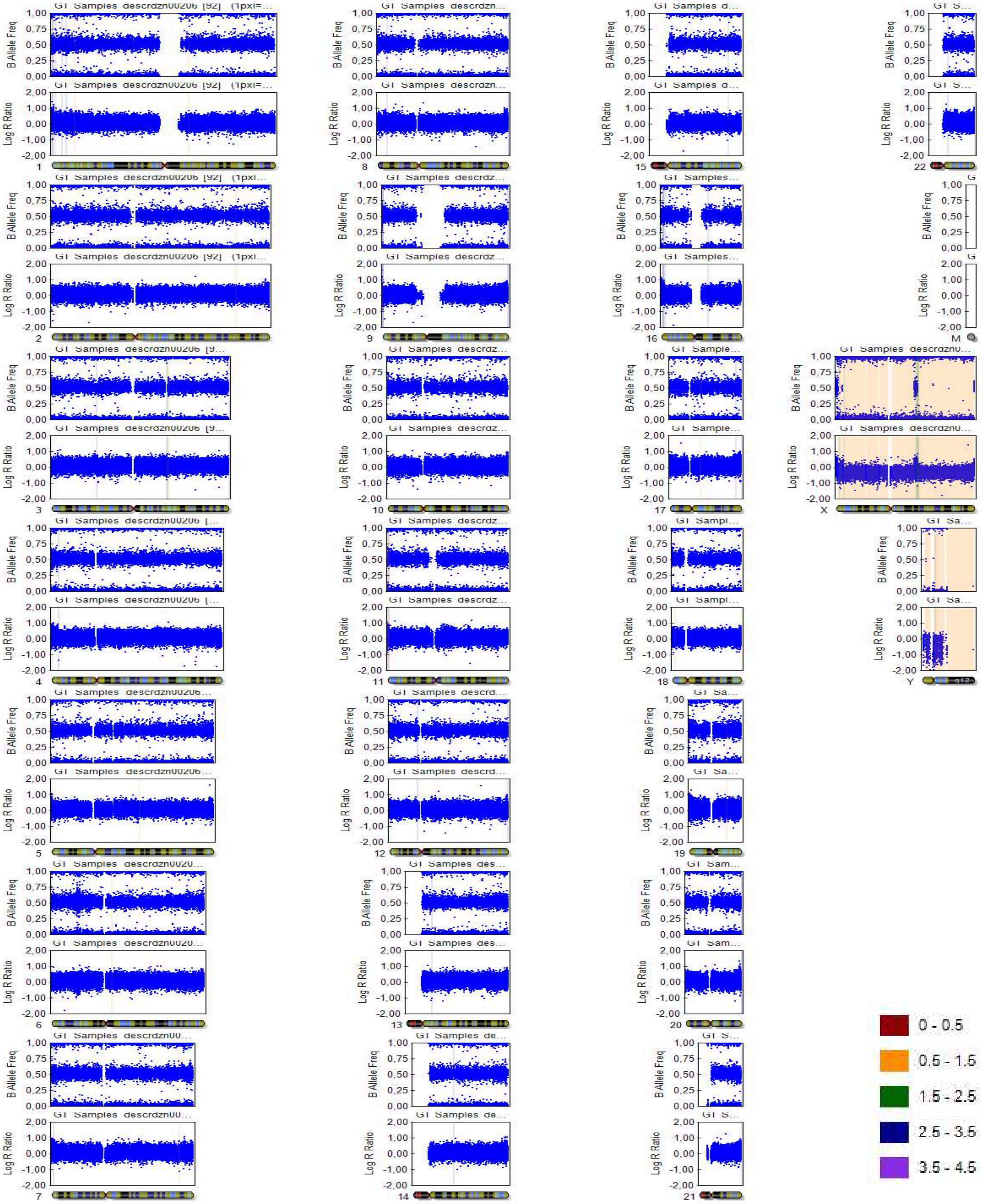
GT Samples descrdzn00206 [92] (1pxl=...
B Allele Freq
Log R Ratio
1,00
0,75
0,50
0,25
0,00
2,00
1,00
0,00
-1,00
-2,00
1
2
3
4
5
6
7
8
9
10
11
12
13
14
15
16
17
18
19
20
21
22
X
Y
M
0 - 0.5
0.5 - 1.5
1.5 - 2.5
2.5 - 3.5
3.5 - 4.5

Copy Number Analysis

Copy number events will be reported if larger than 350'000 base pairs, 1Mbp for loss of heterozygosity regions.
Database of Genomic Variants comparison: Number stated represent population based copy number variants that span the reported event completely.

Copy number analysis

Algorithm applied: CNV-Partition
Version: 3.2
Software producer: Illumina, Inc., San Diego, United States of America

Sample ID	**Chr**	**Start**	**End**	**Type**	**Length**	**Marker count**	**CN Confidence**	**DGV Comparison**
DESCRDZN00206	3	127465894	129762545	2	2296651	1816	283,233	

Karyotype Report

Customer sample ID: iPS-PCH-02_1.7_p10
Internal sample ID: DE07SCRDZND100207
Date of receipt: 2021-03-09

Gender
Stated: Unstated
Chr. X derived: Male

Genotype identity with: F-PCH-02_P5-2021-03-09 / DESCRDZN00203,
IPS-PCH-02_4.1_P11-2021-03-09 / DESCRDZN00208

Karyotyping

Technology used: Illumina BeadArray

Product: HumanOmni2.5Exome-8 BeadChip v1.5
Manifest file: InfiniumOmni2-5Exome-8v1-5_A1.bpm
Cluster file: InfiniumOmni2-5Exome-8v1-5_A1-Cluster-File.egt

Chip barcode and segment: 204372050103 R08C01

Batch ID and 96 well position: WG6917121-MSA6 H02

Call rate: 0,9970004

Typing
Scanner: Illumina iScan, S/N: N234
Site of processing: Life&Brain GENOMICS, Bonn, Germany
Manufacturer: Illumina, Inc., San Diego, United States of America
Date of scan: 2021-03-17-1200

Genotype Analysis
Genome Studio: GenomeStudio V2.0.5
Genotyping module: Ver. 2.0.5

Copy Number Analysis
Algorithm applied: CNV-Partition
Version: 3.2.0
Software producer: Illumina, Inc., San Diego, United States of America

Noteworthy findings

No larger chromosomal aberrations to be reported.

Control Dashboard

Sample_ID / Sentrix_Label	Category	Control (BeadType)	Section 1 X	Section 1 Y	State
DESCRDZN00207 / 204372050103_R08C01	Staining	DNP (High) (27630314)	43484	373	OK/OK
DESCRDZN00207 / 204372050103_R08C01	Staining	DNP (Bgnd) (43603326)	813	392	Notable/ Notable
DESCRDZN00207 / 204372050103_R08C01	Staining	Biotin (High) (41666334)	1013	24996	Notable/OK
DESCRDZN00207 / 204372050103_R08C01	Staining	Biotin (Bgnd) (34648333)	743	362	Notable/OK
DESCRDZN00207 / 204372050103_R08C01	Extension	Extension (A) (17616306)	39698	614	OK/OK
DESCRDZN00207 / 204372050103_R08C01	Extension	Extension (T) (14607337)	40283	498	OK/OK
DESCRDZN00207 / 204372050103_R08C01	Extension	Extension (C) (12613307)	1959	25122	OK/OK
DESCRDZN00207 / 204372050103_R08C01	Extension	Extension (G) (11603365)	2321	25291	Notable/OK
DESCRDZN00207 / 204372050103_R08C01	Target Removal	Target Removal (31623323)	1360	398	OK/OK
DESCRDZN00207 / 204372050103_R08C01	Hybridization	Hyb (High) (19612319)	1643	25731	OK/OK
DESCRDZN00207 / 204372050103_R08C01	Hybridization	Hyb (Medium) (20636378)	876	17961	OK/OK
DESCRDZN00207 / 204372050103_R08C01	Hybridization	Hyb (Low) (23617335)	1879	4195	OK/OK
DESCRDZN00207 / 204372050103_R08C01	Stringency	String (PM) (32629312)	28809	621	OK/OK
DESCRDZN00207 / 204372050103_R08C01	Stringency	String (MM) (33668307)	6714	417	Notable/OK
DESCRDZN00207 / 204372050103_R08C01	Non-Specific Binding	NSB (Bgnd) (28637363)	719	402	Notable/OK
DESCRDZN00207 / 204372050103_R08C01	Non-Specific Binding	NSB (Bgnd) (27624356)	691	344	OK/OK
DESCRDZN00207 / 204372050103_R08C01	Non-Specific Binding	NSB (Bgnd) (25617343)	661	380	OK/OK
DESCRDZN00207 / 204372050103_R08C01	Non-Specific Binding	NSB (Bgnd) (24616350)	699	357	OK/OK
DESCRDZN00207 / 204372050103_R08C01	Non-Polymorphic	NP(A) (34633358)	12123	492	OK/OK
DESCRDZN00207 / 204372050103_R08C01	Non-Polymorphic	NP(T) (16648324)	19309	448	OK/OK
DESCRDZN00207 / 204372050103_R08C01	Non-Polymorphic	NP(C) (43641328)	951	13059	OK/OK
DESCRDZN00207 / 204372050103_R08C01	Non-Polymorphic	NP(G) (13642359)	961	12365	OK/OK

All „Notable“ tagged probes are within specs. The karyogram can be evaluated.

Karyogram

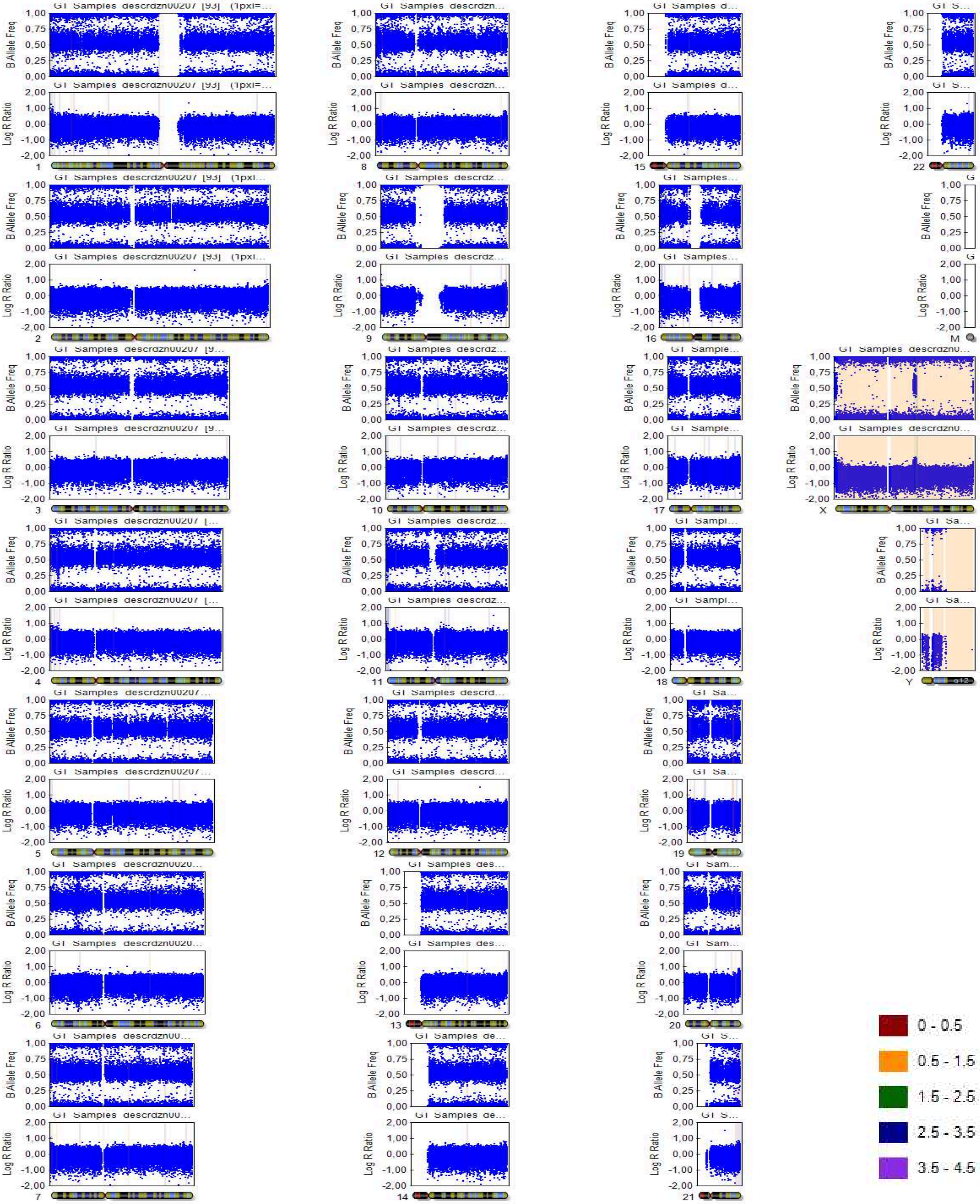
GT Samples descrdzn00207 [93] (1pxl=…
B Allele Freq
1,00
0,75
0,50
0,25
0,00
Log R Ratio
2,00
1,00
0,00
-1,00
-2,00
1
2
3
4
5
6
7
8
9
10
11
12
13
14
15
16
17
18
19
20
21
22
M
X
Y
q12
0 - 0.5
0.5 - 1.5
1.5 - 2.5
2.5 - 3.5
3.5 - 4.5

Copy Number Analysis

Copy number events will be reported if larger than 350'000 base pairs, 1Mbp for loss of heterozygosity regions.
Database of Genomic Variants comparison: Number stated represent population based copy number variants that span the reported event completely.

Copy number analysis

Algorithm applied: CNV-Partition
Version: 3.2
Software producer: Illumina, Inc., San Diego, United States of America

Sample ID	**Chr**	**Start**	**End**	**Type**	**Length**	**Marker count**	**CN Confidence**	**DGV Comparison**
DESCRDZN00207	4	9558683	10407505	3	848822	710	2740,706	

Karyotype Report

Customer sample ID: iPS-PCH-03_4.2_p10
Internal sample ID: DE50SCRDZND100209
Date of receipt: 2021-03-09

Gender
Stated: Unstated
Chr. X derived: Male

Genotype identity with: F-PCH-03_P2-2021-03-09 / DESCRDZN00204, IPS-PCH-03_6.1_P11-2021-03-09 / DESCRDZN00210

Karyotyping

Technology used: Illumina BeadArray

Product: HumanOmni2.5Exome-8 BeadChip v1.5
Manifest file: InfiniumOmni2-5Exome-8v1-5_A1.bpm
Cluster file: InfiniumOmni2-5Exome-8v1-5_A1-Cluster-File.egt

Chip barcode and segment: 204372060010 R02C01

Batch ID and 96 well position: WG6917121-MSA6 B03

Call rate: 0,9982454

Typing
Scanner: Illumina iScan, S/N: N234
Site of processing: Life&Brain GENOMICS, Bonn, Germany
Manufacturer: Illumina, Inc., San Diego, United States of America
Date of scan: 2021-03-17-1200

Genotype Analysis
Genome Studio: GenomeStudio V2.0.5
Genotyping module: Ver. 2.0.5

Copy Number Analysis
Algorithm applied: CNV-Partition
Version: 3.2.0
Software producer: Illumina, Inc., San Diego, United States of America

Noteworthy findings

No larger chromosomal aberrations to be reported.

Control Dashboard

Sample_ID / Sentrix_Label	Category	Control (BeadType)	Section 1 X	Section 1 Y	State
DESCRDZN00209 / 204372060010_R02C01	Staining	DNP (High) (27630314)	30251	86	OK/OK
DESCRDZN00209 / 204372060010_R02C01	Staining	DNP (Bgnd) (43603326)	339	156	Notable/ Notable
DESCRDZN00209 / 204372060010_R02C01	Staining	Biotin (High) (41666334)	465	11921	OK/OK
DESCRDZN00209 / 204372060010_R02C01	Staining	Biotin (Bgnd) (34648333)	363	141	OK/OK
DESCRDZN00209 / 204372060010_R02C01	Extension	Extension (A) (17616306)	26250	248	OK/OK
DESCRDZN00209 / 204372060010_R02C01	Extension	Extension (T) (14607337)	27511	254	OK/OK
DESCRDZN00209 / 204372060010_R02C01	Extension	Extension (C) (12613307)	1074	12240	OK/OK
DESCRDZN00209 / 204372060010_R02C01	Extension	Extension (G) (11603365)	1331	11312	OK/OK
DESCRDZN00209 / 204372060010_R02C01	Target Removal	Target Removal (31623323)	643	156	OK/OK
DESCRDZN00209 / 204372060010_R02C01	Hybridization	Hyb (High) (19612319)	1131	12010	OK/OK
DESCRDZN00209 / 204372060010_R02C01	Hybridization	Hyb (Medium) (20636378)	414	8273	OK/OK
DESCRDZN00209 / 204372060010_R02C01	Hybridization	Hyb (Low) (23617335)	998	2530	OK/OK
DESCRDZN00209 / 204372060010_R02C01	Stringency	String (PM) (32629312)	18022	296	OK/OK
DESCRDZN00209 / 204372060010_R02C01	Stringency	String (MM) (33668307)	5625	182	OK/OK
DESCRDZN00209 / 204372060010_R02C01	Non-Specific Binding	NSB (Bgnd) (28637363)	358	156	OK/OK
DESCRDZN00209 / 204372060010_R02C01	Non-Specific Binding	NSB (Bgnd) (27624356)	336	162	OK/OK
DESCRDZN00209 / 204372060010_R02C01	Non-Specific Binding	NSB (Bgnd) (25617343)	347	184	OK/OK
DESCRDZN00209 / 204372060010_R02C01	Non-Specific Binding	NSB (Bgnd) (24616350)	286	178	OK/OK
DESCRDZN00209 / 204372060010_R02C01	Non-Polymorphic	NP(A) (34633358)	8841	256	OK/OK
DESCRDZN00209 / 204372060010_R02C01	Non-Polymorphic	NP(T) (16648324)	12595	230	OK/OK
DESCRDZN00209 / 204372060010_R02C01	Non-Polymorphic	NP(C) (43641328)	549	6457	OK/OK
DESCRDZN00209 / 204372060010_R02C01	Non-Polymorphic	NP(G) (13642359)	644	6025	OK/OK

All „Notable“ tagged probes are within specs. The karyogram can be evaluated.

Karyogram

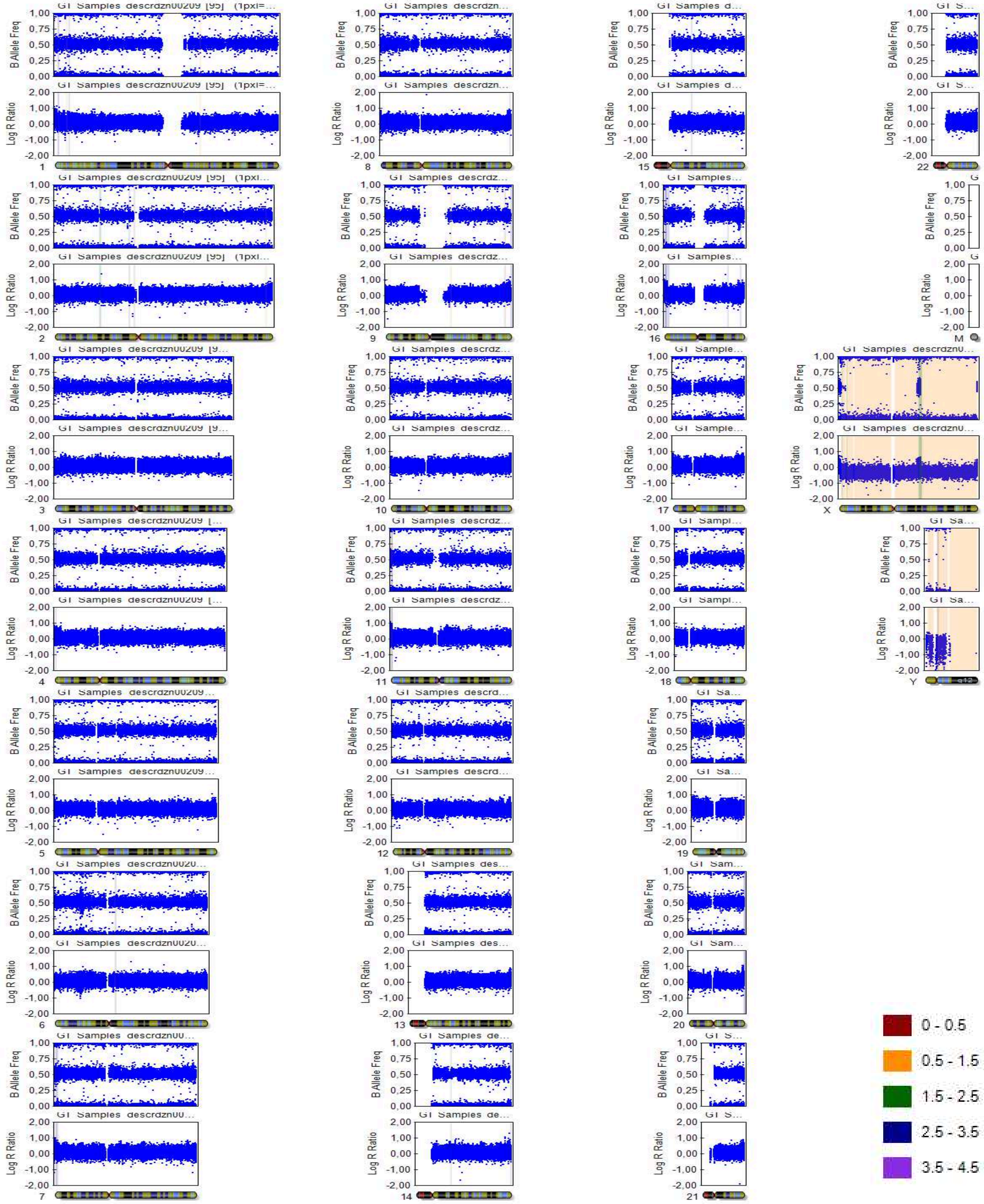
GT Samples descrdzn00209 [95]
B Allele Freq
Log R Ratio
1,00
0,75
0,50
0,25
0,00
2,00
1,00
0,00
-1,00
-2,00
1
2
3
4
5
6
7
8
9
10
11
12
13
14
15
16
17
18
19
20
21
22
M
X
Y
G
q12
🟥 0 - 0.5
🟧 0.5 - 1.5
🟩 1.5 - 2.5
🟦 2.5 - 3.5
🟪 3.5 - 4.5

Copy Number Analysis

Copy number events will be reported if larger than 350'000 base pairs, 1Mbp for loss of heterozygosity regions.
Database of Genomic Variants comparison: Number stated represent population based copy number variants that span the reported event completely.

Copy number analysis

Algorithm applied: CNV-Partition
Version: 3.2
Software producer: Illumina, Inc., San Diego, United States of America

Sample ID	Chr	Start	End	Type	Length	Marker count	CN Confidence	DGV Comparison
DESCRDZN00209	2	49977093	52048553	2	2071460	1910	481,6987	
DESCRDZN00209	14	38487404	40341185	2	1853781	1534	333,2639	